ROYAL SOCIETY OF CHEMISTRY

Check for updates

Recoverable aggregate-rich liquefied gas electrolytes for enabling high-voltage lithium metal batteries

Ganesh Raghavendran, [iD] †[a] Alex Liu, [iD] †[a] Oleg Borodin,[b] Nathan Hahn, [iD] [c] Kevin Leung, [iD] [c] Na-Ri Park,[a] Tejas Nivarty, [iD] [a] Mingqian Li,[a] Aiden Larson,[a] Yijie Yin, [iD] [d] Minghao Zhang [iD] *[e] and Ying Shirley Meng [iD] *[ae]

High-energy density, improved safety, temperature resilience, and sustainability are desirable yet rarely simultaneously achieved properties in lithium-battery electrolytes. In this work, we present an aggregate-rich electrolyte that leverages the complementary features of ionic liquids and liquefied gas solvents, achieving a high conductivity of 17.7 mS cm^{-1} at room temperature. The aggregate-rich solvation chemistry and enhanced fluidity result in superior performance of 20 μm Li/NMC811 full cell batteries with 90.41% capacity retention at 4.4 V, 80% capacity retention after 150 cycles, and enhanced low-temperature compatibility until −60 °C. Additionally, we demonstrate a conceptual workflow for recovering individual electrolyte components, contributing to the circularity of batteries. This work provides a pathway to sustainable, temperature-resilient high-voltage (>4.4 V) lithium–metal batteries that maintain state-of-the-art electrochemical performance, potentially advancing the development of next-generation energy storage systems.

Broader context

The transition to sustainable energy systems demands advanced lithium–metal batteries capable of exceeding 500 Wh kg^{-1} while operating reliably across extreme temperatures and voltages above 4.4 V. However, conventional electrolytes face fundamental limitations: carbonate-based systems suffer from poor thermal stability and safety concerns, while ionic liquids, despite excellent electrochemical stability, exhibit prohibitively high viscosities that hinder practical implementation. This creates a critical bottleneck in achieving next-generation energy storage performance. Our ionic liquid-liquefied gas electrolyte (IL-LGE) addresses these challenges through rational solvation structure engineering that synergistically combines the high-voltage stability of ionic liquids with the exceptional fluidity of liquefied gas solvents. By creating aggregate-rich solvation structures with minimal free anions, the IL-LGE enables anion-derived solid electrolyte interphase formation while maintaining high ionic conductivity. This approach enables stable operation at temperatures as low as −60 °C while maintaining superior performance at voltages exceeding 4.4 V—capabilities that are rarely achieved simultaneously in existing systems. By demonstrating a recovery workflow for individual electrolyte components, we contribute to the circular economy in energy storage, offering a pathway toward environmentally responsible battery systems that meet both performance and sustainability requirements for future applications.

Introduction

The demand for high-performance and energy-dense secondary batteries has surged in recent decades, driven by their

[a] *Aiiso Yufeng Li Family Department of Chemical and Nano Engineering, University of California San Diego, La Jolla, CA, 92093, USA*

[b] *Battery Sciences Branch, Energy Science Division, DEVCOM Army Research Laboratory, Adelphi, MD, 20783, USA*

[c] *Sandia National Laboratories, Albuquerque, NM, 87123, USA*

[d] *Materials Science and Engineering, University of California San Diego, La Jolla, CA, 92093, USA*

[e] *Pritzker School of Molecular Engineering, University of Chicago, Chicago, IL, 60637, USA. E-mail: miz016@uchicago.edu, shirleymeng@uchicago.edu*

† Co-first authors.

expanding applications in portable electronics, electric vehicles, and renewable energy systems.[1] To meet this demand, significant effort has been dedicated to developing electrodes and electrolytes for operation at extreme potentials. The Li metal anode is a compelling alternative to the conventional graphite anode in today's lithium-ion batteries, offering a much higher theoretical specific capacity (3860 mAh g^{-1} *vs.* 372 mAh g^{-1}) and a low standard reduction potential (−3.04 V *versus* the standard hydrogen electrode), essential for achieving the rigorous gravimetric energy density requirements of next-generation secondary batteries (>500 Wh kg^{-1}). However, the practical implementation of lithium–metal batteries (LMBs) has been hindered by persistent safety concerns particularly those related to dendritic growth, as well as limited cycle life. These challenges have

This journal is © The Royal Society of Chemistry 2025

Energy Environ. Sci., 2025, **18**, 8889–8906 | 8889

motivated extensive efforts in electrolyte engineering and inter-face design.

While carbonate-based electrolytes are usually considered for high voltage Li-ion systems, poor reduction stability and the formation of un-favorable SEI have made them unsuitable for high-V Li metal batteries. Though ether-based electrolytes are compatible with Li metal, the poor oxidation stability of ether solvents poses a challenge for enabling high voltage Li metal batteries.[2,3] Super-concentrated ether-based electrolytes have demonstrated favorable passivation of the Li metal anode while offering anodic stability against 5 V class cathodes.[4,5] The design principles of these high-concentration electrolytes (HCEs) rely on enhanced anion participation in the solvation structures. Stemming from the competitive coordination between solvent and anion ligands with Li⁺, increased anion-rich solvation structures naturally lead to an anion-derived solid electrode–electrolyte interphase (SEI). Anion-derived SEI are generally composed primarily of inorganic lithium compounds (e.g. LiF, Li_2O, etc.), widely reported as beneficial for Li metal anodes due to their mechanical strength and ease of Li lateral diffusion across the interface.[6–8] In addition to the dependency of interfacial chemistry on electrolyte solvation structure, increased anion participation facilitates superior anodic stability due to lower solvent activity, mitigating the deleterious cathode–electrolyte side reaction.[9,10]

Nevertheless, these electrolyte systems face significant limitations, primarily due to their requirement for high salt concentrations to engineer anion-rich solvation structures, which substantially increases production costs. Additionally, these electrolytes typically exhibit sluggish transport properties due to their high viscosity, resulting in practical limitations such as poor wettability.[11] To address these issues, localized high-concentration electrolytes (LHCEs) were developed by diluting HCEs with inert solvents – this approach reduces viscosity and production costs, while retaining the core functionality of the HCE.[12]

Although exploited in HCEs to mitigate their intrinsically low anodic stabilities (<4 V), conventional liquid organic solvents still suffer from mass transport limitations and intrinsic flammability.[13] In the context of recycling, aged battery electrolytes decompose during the thermal pretreatment step of pyro- and hydrometallurgical processes, where volatile organic liquid solvents decompose into a series of alcohols and aldehydes.[14,15] These byproducts readily diffuse into water, soil, and air, causing severe environmental contamination, an issue compounded by the fact that electrolytes account for 10–15 wt% of batteries.[16]

In contrast, ionic liquid (IL) solvents, comprised of cation–anion pairs, offer both wider chemical and electrochemical stability.[17,18] The presence of ion-pairs enables the tuning of electrolyte microstructures and SEI. Furthermore, their non-volatility due to intrinsically negligible vapor pressure, and ultra-high thermal stability (>250 °C) facilitate solvent recovery more efficiently compared to volatile organic solvents.[19] However, their applications as single solvents in electrolytes have largely been impeded by their typically high viscosity, resulting in poor wettability of electrode materials. Regarding

the ionic conductivity, ILs exhibit a broad range of room temperature ionic conductivities from 0.1–18 mS cm⁻¹,[20] but applications as electrolyte solvents in Li battery systems may be hindered by the negative correlation between ionic conductivity and Li-salt concentrations.[21] As for Li⁺ transference, the net mobility of Li⁺ as solved by ILs tends to be low, due to strong ion–ion interactions.[22] Consequently, inert co-solvents were employed to improve upon the transport and rheological properties of IL-based electrolytes by means of dilution as an LHCE.[23] Nevertheless, LHCEs based on ILs still exhibit sub-par Li⁺ transference and poor low-temperature performance.[24]

Circumventing the conventional liquid-phase temperature window, liquefied gas electrolytes (LGEs) based on hydrofluoro-carbons (e.g., fluoromethane, difluoromethane, etc.) have been reported to demonstrate exceptionally low viscosities, yielding relatively high ionic conductivities even with moderate dielectric constants.[25] Moreover, exceptional compatibility with Li metal anodes has been demonstrated when paired with organic solvents such as tetrahydrofuran, 1,2-dimethoxyethane or acetonitrile as an LHCE.[25–27] Compared to commonly reported LHCEs in the literature, which employ inert hydrofluoroether diluents such as bis(2,2,2-trifluoroethyl) ether or 2,2,2-trifluoroethyl-1,1,2-tetra-fluoroethyl ether, liquefied gas diluents are more easily recovered.[28] This is significant as many hydrofluoroether dilu-ents contain perfluoroakyl groups, classifying them as 'forever chemicals' with unsustainable environmental impacts.[29] As such, it is expected that when paired with high concentration IL-based electrolytes, liquefied gas solvents could help overcome the bottlenecks of using IL-based electrolytes such as high viscosity and poor low temperature performance while retaining core functionalities such as high anodic stability and propensity to form anion-derived SEIs.

Herein, we report an ionic-liquid based LGE (IL-LGE) and explore the approach of minimizing salt utilization in electrolyte engineering through the rational design of an IL-based LGE based on N-methyl-N-propyl-pyrrolidinium bis(trifluoromethane)sulfo-nimide (Pyr₁₃-TFSI) and fluoromethane (FM). We demonstrate the ability to engineer the desired anionic solvation structures for the stable cycling of high voltage Ni-rich layered oxide LiNi₀.₈-Mn₀.₁Co₀.₁O₂ (NMC811) cathodes with 20 μm lithium metal anodes exhibiting 91.48% capacity retention at a cutoff voltage of 4.4 V after 150 cycles. A conventional electrolyte of 1.0 M $LiPF_6$ in EC/EMC (3:7 wt%) + 2 wt% VC was selected as the baseline electrolyte (hereinafter, baseline), demonstrating 27.13% capacity retention under identical cycling conditions. Inductively coupled plasma mass spectrometry (ICP-MS) reveals suppression of Ni and Mn dissolution using the designed IL-LGE electrolyte, an issue exacerbated in Ni-rich NMCs.[30] Detailed analysis of interfacial chemistry at the cathode surface and anode was conducted using X-ray photoelectron spectroscopy (XPS) and correlated with an electrolyte structure obtained from molecular dynamics (MD) simulation and complemented by density functional theory (DFT) studies of electrolyte–cathode interfaces. Additionally, the conceptual workflow for recovering the formulated electrolyte components is demonstrated and validated.

Results and discussions

Electrolyte design rationale for high voltage Li metal batteries

Wide electrochemical window of the electrolyte is one of the key criteria for enabling high voltage Li metal batteries. The design principle of engineering anion-rich solvation structures is adopted in this work, a strategy known to significantly extend the electrochemical stability window of electrolytes. While voltage stability can be enhanced through highly aggregated systems, ionic transport properties are typically compromised—creating a fundamental design bottleneck that must be addressed. To realize this design, ILs are utilized as solvents, which, being composed entirely of ions, facilitate solvation structure engineering. Suitable ILs that can facilitate the formation of anion-rich aggregates are being screened, along with co-solvents that can complement these ILs, with the design goal of achieving both the desired transport properties and high voltage stability. Three main design criteria were considered in the electrolyte design: the electrochemical windows of the electrolyte components, their transport properties, and the propensity to achieve an aggregate-rich structure. Fig. 1 presents a comprehensive comparison of three electrolyte classes —ILs, organic solvents, and liquefied gas solvents—analyzing their physical properties that influence performance in Li metal battery systems.

Electrolyte decomposition at high voltage does not always proceed *via* direct electron transfer from electrolyte components to the cathode surface. Dehydrogenation of carbonate solvents has been identified as one of the primary decomposition pathways of the electrolytes in high voltage systems.[34] Decomposition of electrolyte species at the cathode surface is sometimes preferred, which contributes to the formation of a stable cathode–electrolyte interface.[35,36] For preliminary screening of electrolyte components, the highest occupied molecular orbital (HOMO) and lowest unoccupied molecular orbital (LUMO) energy levels are used in our work for simplicity and convenience. ILs consistently demonstrate low HOMO values, particularly those with the N-propyl-N-methyl-pyrrolidinium (Pyr_{13}^+) cation, indicating superior oxidative stability. While butyl-(BMIM$^+$) and ethyl-imidazolium (EMIM$^+$) cations show comparable HOMO values, they suffer from poor reduction stability.[37] Organic liquid solvents, such as DME, DfbN, EC, EMC, and PC, generally exhibit intermediate HOMO values. In contrast, liquefied gas solvents like FM, DFM, and TFE display higher oxidative stability based on HOMO values (Section S3 and Table S1).

The dielectric-fluidity factor ($\varepsilon_r \times \eta^{-1}$), which is the ratio of the dielectric constant (ε_r) to the viscosity (η), serves as an indicator of the electrolyte's ability to effectively dissolve and transport lithium ions (Fig. 1a).[25] The viscosity and the dielectric constants of the considered solvents were obtained from the literature.[25,38–44] While ILs exhibit extremely low $\varepsilon_r \cdot \eta^{-1}$ values due to their very high viscosity, the values of liquefied gas solvents are orders of magnitude higher than those for ILs and liquid organic solvents, particularly FM and DFM. Although the dielectric constant of FM and DFM are low, indicative of poor salt solubility, they exhibit exceptionally low viscosities which enable higher ion conduction when used as co-solvents.

Electrostatic potential mapping and Li$^+$ binding energy calculations for organic and liquefied gas solvents were used to screen co-solvents that minimize solvent participation in the solvation structure while preserving the anion-rich solvation environment. The decreasing Li$^+$ solvation trend from PC to TFE correlates with the electron-donating capabilities of these solvents and their ability to coordinate with lithium ions. FM (ESP$_{min}$ = −0.97 eV), DFM (ESP$_{min}$ = −0.87 eV), DfbN (ESP$_{min}$ = −0.85 eV)
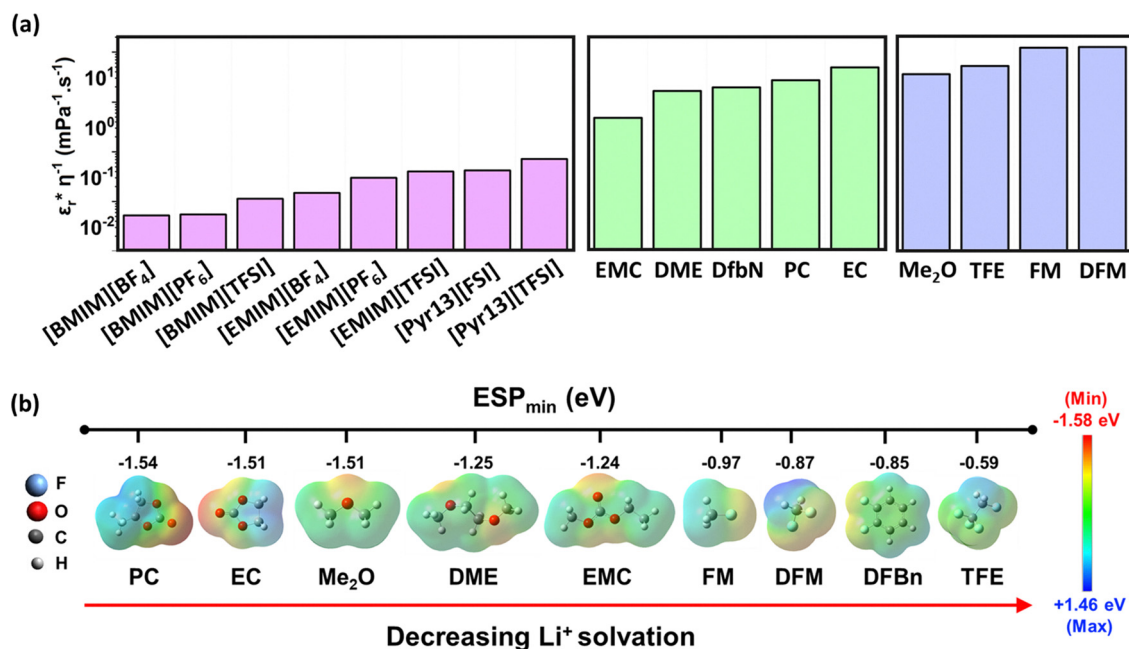

Fig. 1 Comparison of (a) dielectric-fluidity ($\varepsilon_r \times \eta^{-1}$) factor values of ILs (pink), organic solvents (green), and liquefied gas solvents (blue) – calculated from the literature [ref. 13 and 18–24]. (b) ESP mapping minima and Li$^+$ solvating power screening of organic and liquefied gas solvents.

and TFE ($ESP_{min} = -0.59$ eV) exhibit potential low Li$^+$ solvation properties due to their more delocalized electron density (Fig. 1b). The limited Li$^+$ solvation properties facilitate the engineering of an aggregate-rich solvation structure by compelling anion participation in the solvation process. This is achieved by creating an environment where the electrolyte is deficient in solvating solvents, thereby promoting the formation of ion aggregates.

Out of the solvents screened, FM, DFM and TFE were chosen due to their exceptionally high voltage stability, high dielectric-fluidity factor, and propensity to preserve aggregate-rich solvation structures. Regarding ILs, the pyrrolidium cation was chosen for its wide electrochemical stability window, while TFSI$^-$ and FSI$^-$ anions were considered due to their relatively lower viscosity and better stability against moisture compared to the PF$_6^-$ and BF$_4^-$ anions.[45,46]

IL-LGE electrolyte formulation and optimization

The selected co-solvents for electrolyte formulation after screening included FM, DFM, and TFE. The ILs under consideration were Pyr$_{13}$TFSI and Pyr$_{13}$FSI. Although LiPF$_6$ is widely employed as an electrolyte salt for high-voltage applications, it exhibits poor moisture compatibility. In the presence of even trace amounts of moisture, LiPF$_6$ undergoes hydrolysis, generating corrosive HF as a byproduct, which subsequently leads to cathode material degradation.[35,47,48] In contrast, imide-based salts such as LiTFSI and LiFSI demonstrate not only resistance to hydrolysis but also enhanced dissociation in organic solvents due to their highly conjugated anionic centers (–SO$_2$–N–SO$_2$–), enabling better ionic conductivities and thermal stability compared to conventional electrolyte salts.[49,50] LiTFSI and LiFSI were chosen as the lithium salts due to their better moisture stability, enhanced solubility, higher conductivity and potential to facilitate high-voltage lithium metal battery systems.[51] While Al corrosion is reported as one of the issues related to usage of perfluoroalkylsulfonyl imide based salts,[52] our electrolyte design addresses this issue, which is detailed in the later sections.

The miscibility of liquefied gas solvents with IL mixtures was investigated using Pyr$_{13}$TFSI/FSI combined with Li-TFSI/FSI salt mixtures at a 1:1 molar ratio. These mixtures were tested with liquefied gas solvents at a molar ratio of 1:1:5 (salt:IL:liquefied gas solvent) as illustrated in Fig. 2a. While DFM and TFE exhibited phase separation with the IL–salt mixtures (Fig. S3 and Section S4), FM demonstrated miscibility exclusively with LiTFSI salt mixtures. Although FSI$^-$-based ILs are generally favored for their compatibility with lithium metal[53] and lower viscosity,[54] Pyr$_{13}$TFSI was chosen over Pyr$_{13}$FSI due to its superior voltage stability[55] and cost-effectiveness.[56] Additionally, the
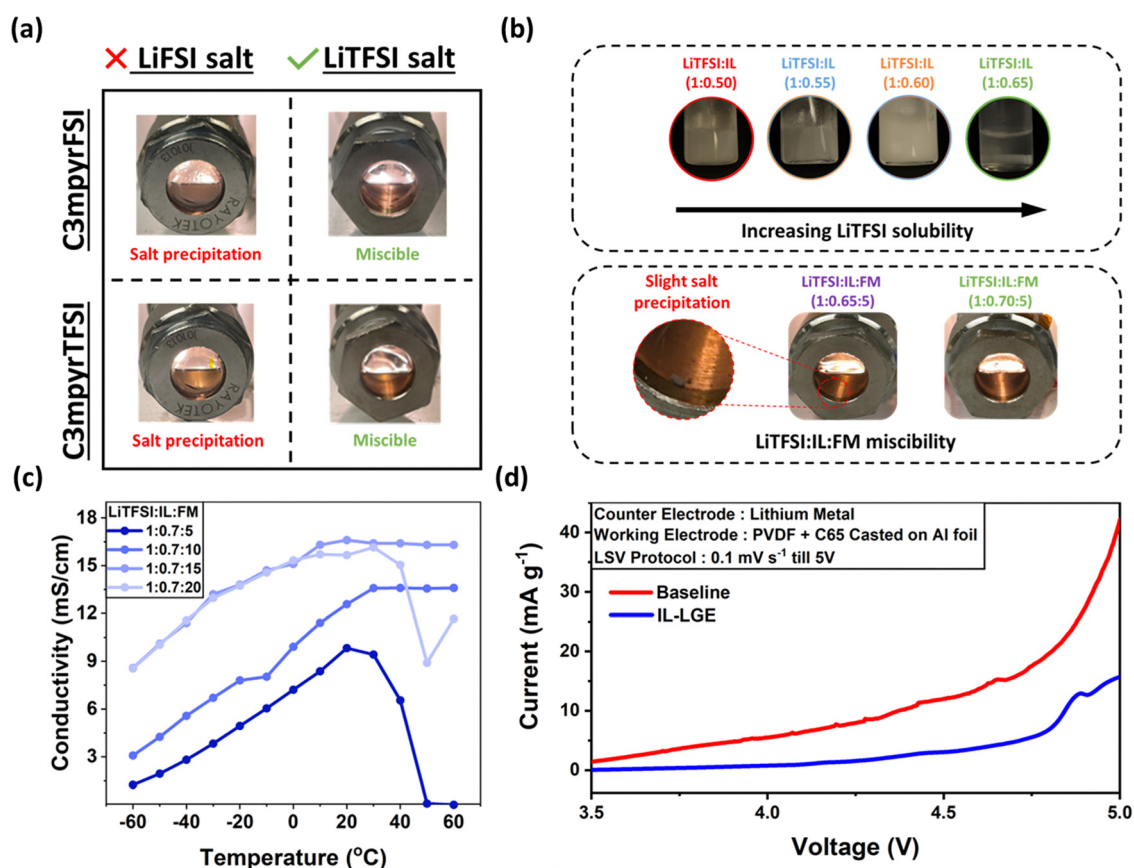

Fig. 2 (a) Miscibility chart of FM with mixtures of FSI and TFSI anion-based ILs and Li salts. (b) Solubility screening of LiTFSI salt in TFSI anion-based IL. (c) Ionic conductivity-based optimization of the LGEs over a wide temperature range. (d) Linear sweep voltammetry experiment with baseline and IL-LGE electrolyte.

8892 | *Energy Environ. Sci.*, 2025, **18**, 8889–8906

This journal is © The Royal Society of Chemistry 2025

use of CO_2 with FM as an additive has been previously reported to enhance lithium metal cycling performance.[57] In this study, the CO_2 additive was similarly utilized to enhance lithium metal compatibility, as detailed in later sections of the paper.

The solubility limit of LiTFSI in Pyr_{13}TFSI was investigated to determine the optimal concentration for achieving aggregate-rich solvation structures at saturation. Although the solubility limit of LiTFSI in Pyr_{13}TFSI was initially determined to be $1:0.65$ (molar ratio), the addition of FM resulted in slight salt precipitation. Consequently, the molar ratio was adjusted to $1:0.70$ to obtain a fully miscible solution, as illustrated in Fig. 2b. Addition of FM in this concentrated mixture yielded a stable liquid phase solution across a wide temperature range from $-60\,°C$ to $40\,°C$ (Fig. S4 and Section S4).

Ionic conductivity measurements were performed across a wide temperature range (-60 to $60\,°C$) to evaluate the performance characteristics of various LiTFSI:IL:FM ratios (Fig. 2c). The optimal formulation ($1:0.7:15$) exhibits superior conductivity throughout the entire temperature range, demonstrating a conductivity of $17.7\ mS\ cm^{-1}$ at $20\,°C$. This value represents the highest reported conductivity for an IL-based Li electrolyte system.[58] In comparison, the baseline electrolyte displays a conductivity of $9.7\ mS\ cm^{-1}$ at $20\,°C$. Notably, the optimized IL-LGE maintains a conductivity above $8\ mS\ cm^{-1}$ even at $-60\,°C$, marking the lowest operational temperature reported for an IL-based Li electrolyte.[59] The formulation with a ratio of $1:0.7:20$ exhibits lower conductivity, which is attributed to phase separation within the electrolyte system (Fig. S5 and Section S4). These findings highlight the potential of the optimized IL-LGE formulation for applications requiring high ionic conductivity across a broad temperature range, particularly at low temperatures where traditional electrolytes often fail to perform adequately.[60]

The high voltage stability of the optimized IL-LGE was evaluated in comparison to the baseline electrolyte using an aluminum current collector coated with inactive components of the NMC811 electrode (Super C65 and PVDF binder in a $50:50$ weight ratio). Electrochemical measurements reveal that the IL-LGE system exhibits enhanced voltage stability relative to the baseline electrolyte, demonstrating reduced oxidative current up to $5.0\ V$ (Fig. 2d and Fig. S6, S7 and Section S5). Electrolytes based on $TFSI^-$ anion-rich ILs and highly concentrated solutions containing LiTFSI salts demonstrate electrochemical stability exceeding $5\ V$ *versus* Li, attributed to the inherent high voltage stability of the $TFSI^-$ anion.[61,62] The improved electrochemical stability of IL-LGE formulation at high voltage is attributed to the $TFSI^-$ anion-rich aggregate electrolyte design.

Investigation on the solvation structure of the IL-LGE electrolyte

The solvation structure of the designed IL-LGE was investigated using Raman spectroscopy and molecular dynamics (MD) simulations. A high pressure liquefied gas (HPLG) Raman setup, equipped with an amorphous borosilicate window, was utilized to conduct Raman analysis under high pressure (Fig. 3a). This custom setup demonstrated a wavenumber deviation of

approximately $1\ cm^{-1}$ when benchmarked against a silicon wafer (Fig. S8 and Section S6).

The coordination of Li^+ with $TFSI^-$ was investigated by analyzing the S–N–S bending mode in the Raman spectra of the IL-LGE, LiTFSI:Pyr_{13}TFSI mixture ($1:0.7$ molar ratio), Pyr_{13}TFSI, and LiTFSI salt (Fig. 3b). The addition of LiTFSI salt to Pyr_{13}TFSI results in a blue shift of the peak (from $743.56\ cm^{-1}$ to $746.55\ cm^{-1}$), indicating a more constrained environment for $TFSI^-$ anions. A pronounced blue shift was observed for the IL-LGE peaks ($750.76\ cm^{-1}$) compared to the LiTFSI:Pyr_{13}TFSI mixture ($746.55\ cm^{-1}$) and LiTFSI salt ($747.3\ cm^{-1}$), suggesting a highly aggregated structure and the absence of free $TFSI^-$ anions in the IL-LGE electrolyte. Li^+ coordination with FM was examined by comparing the C–F stretching mode in the Raman spectra of IL-LGE, Pyr_{13}TFSI, and FM (Fig. 3c). A slight blue shift in the IL-LGE electrolyte peaks (from $1010\ cm^{-1}$ to $1015.84\ cm^{-1}$) suggests FM participation in the solvation structure. This involvement of FM potentially explains the more constrained environment of $TFSI^-$ anions, leading to a greater blue shift in the S–N–S bending mode peak of $TFSI^-$. The Pyr_{13}TFSI spectra confirm that the C–F stretching mode of the $TFSI^-$ anion does not overlap with that of FM, validating the observations regarding Li^+ coordination with FM.

Molecular dynamics (MD) simulations were conducted on the IL-LGE electrolyte to gain further insights into the solvation structure and Li^+ environment. Representative snapshots of the MD simulations at 253, 273 and 293 K (Fig. 3d–f) show that the highly aggregated solvation structures are more dispersed than agglomerated, establishing better networks of ionic transport pathways that contribute to the enhanced conductivity observed at room temperature. At 313 K, the ionic networks exhibit increased aggregation and reduced dispersion (Fig. 3g), likely attributed to the proximity to the critical point of FM (317.9 K), resulting in a slight conductivity decrease from $17.7\ mS\ cm^{-1}$ at 293 K to $16.35\ mS\ cm^{-1}$ at 313 K. Based on the RDFs, a first solvation shell cutoff of $2.8\ Å$ was chosen for Li^+ cations, comprising an average of 4.0 O ($TFSI^-$) and 0.95 F (FM) at 293 K. The coordination number remains relatively constant from 253 to 293 K, indicating that the aggregate structure is largely preserved across a wide temperature range (Fig. 3h). Li^+ cations exhibit either bidentate binding to oxygen atoms of $TFSI^-$, resulting in extended chain aggregates, or monodentate binding to oxygen atoms of $TFSI^-$ and fluorine atoms of multiple FM molecules (Fig. 3i). These solvation structures, particularly the participation of FM molecules in Li^+ solvation structures, facilitate Li^+ transport within the electrolyte system, contributing to its enhanced conductivity properties due to the high self-diffusivity exhibited by FM across the temperature range of 253 to 313 K (47.8×10^{-10} to $113.4 \times 10^{-10}\ m^2\ s^{-1}$) (Fig. 3h).

MD simulations predicted conductivity trends in good agreement with experiments (Table S2) albeit slightly overestimating experiments up to 43%. Conductivity starts decreasing below $20\,°C$ due to decreased self-diffusion coefficients and increased viscosity, while ionicity (the inverse Haven's ratio) slightly increases suggesting less ionic correlation due to better
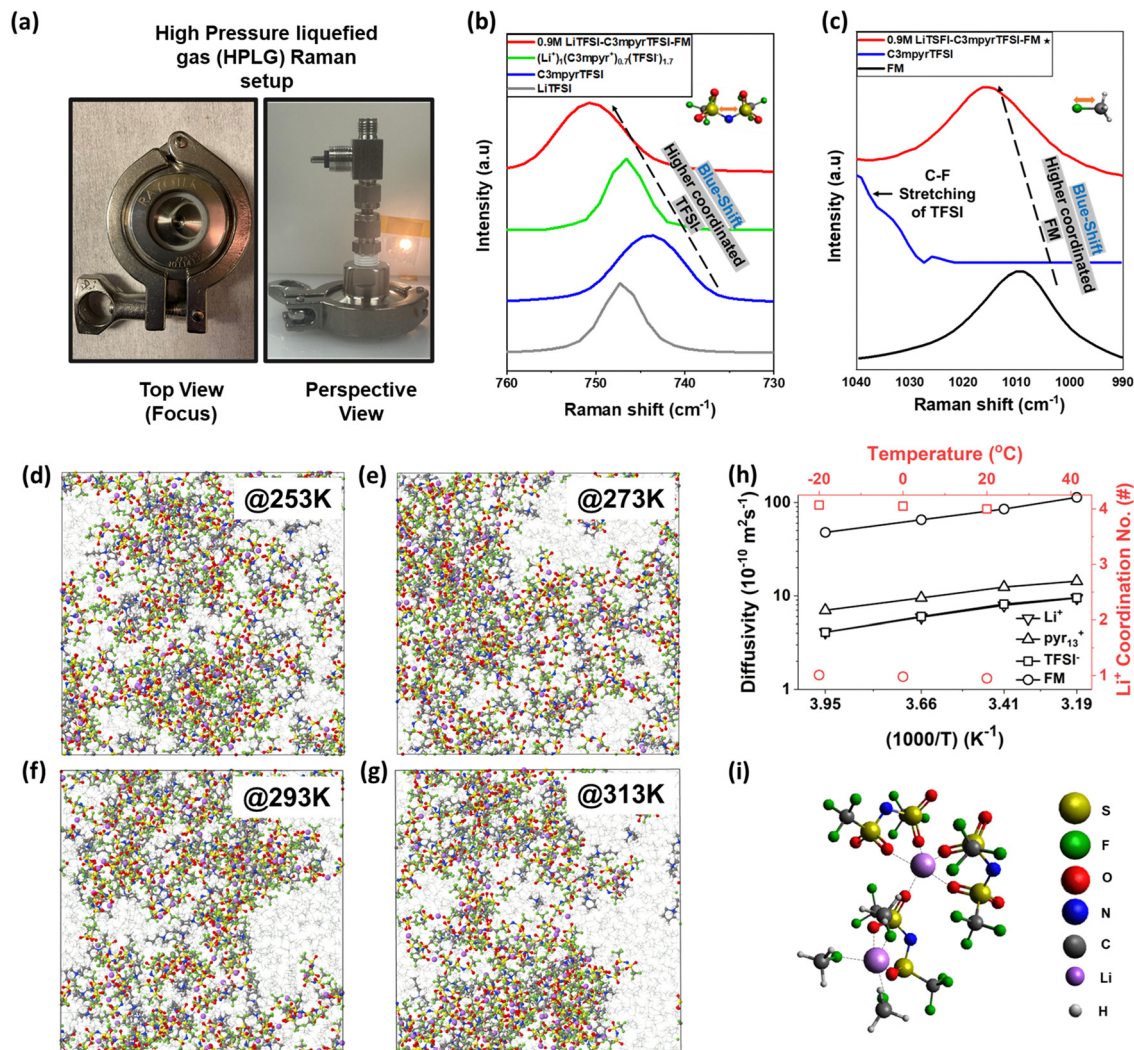
This journal is © The Royal Society of Chemistry 2025

Energy Environ. Sci., 2025, **18**, 8889–8906 | **8893**

Fig. 3 (a) Top and perspective view of the HPLG Raman setup. Raman spectra analysis of IL-LGE, LiTFSI, c3mpyrTFSI and FM probing (b) S−N−S bending mode of TFSI and (c) C−F stretching mode of FM. Representative snapshot of the MD simulation box of IL-LGE at (d) 253 K, (e) 273 K, (f) 293 K, and (g) 313 K. (h) Temperature dependence of diffusivity of electrolyte species and Li$^+$ coordination number. (i) Representative cluster of solvated species of Li$^+$ in IL-LGE.

dissociation at lower temperature. The Li$^+$ and TFSI$^-$ diffused the slowest followed by Pyr$_{13}^+$ with FM showing the fastest diffusion. The self- and distinct contributions to conductivity were calculated. The distinct TFSI$^-$–Li$^+$ σ_d(TFSI$^-$–Li$^+$) contribution (4.5–4.8) is the largest indicating a strong correlation between TFSI$^-$ and Li$^+$ motion as a Li$^+$ is coordinated by 2.4 TFSI$^-$ on average contributing 4 O(TFSI). Because multiple TFSI$^-$ coordinate with a Li$^+$ cation, a distinct σ_d(TFSI$^-$–TFSI$^-$) value > 2 is also significantly observed, indicating correlation of the TFSI$^-$–TFSI$^-$ motion. Interestingly, there is significant correlation between Pyr$_{13}^+$ and TFSI$^-$ with a σ_d(Pyr$_{13}^+$–TFSI$^-$) > 2.0 indicating that due to the ionic neutrality and low dielectric constant of FM, the motion of Pyr$_{13}^+$ correlates with the motion of charged Li$^+$(TFSI$^-$)$_{2.4}$ solvates and aggregates. The Li$^+$ transference number, calculated at 293 K using the diffusion coefficients of Pyr$_{13}^+$, TFSI$^-$, and Li$^+$ (Table S2 and Section S7), is determined to be 0.25–0.27. Experimental measurements using the Bruce–Vincent method[63] yielded a slightly higher value of

0.338 (Fig. S9 and Section S7). The relatively low transference number can be attributed to the higher diffusion rate of Pyr$_{13}^+$ ions compared to Li$^+$ and TFSI$^-$ ions. Despite this low transference number, 'effective Li$^+$ conductivity' – the product of ionic conductivity and transference number, for the IL-LGE electrolyte is 1.82 times that of the baseline electrolyte, suggesting superior rate capability for the IL-LGE system.

Lithium metal anode compatibility with the IL-LGE electrolyte

A soak test of lithium metal in the optimized IL-LGE electrolyte reveals signs of surface corrosion after three days, due to the reactivity of FM with lithium.[25] Previous studies on FM-based LGEs have reported the use of CO$_2$ as an additive to stabilize lithium metal through the formation of Li$_2$CO$_3$. In this study, the CO$_2$ additive concentration was optimized to 1 wt% based on electrolyte miscibility considerations. Subsequent soak tests of lithium metal in the CO$_2$-modified electrolyte show a shiny

8894 | *Energy Environ. Sci.*, 2025, **18**, 8889–8906

This journal is © The Royal Society of Chemistry 2025

lithium surface, indicating effective mitigation of FM-induced corrosion (Fig. S10 and Section S8).

To evaluate the electrochemical performance and compatibility of lithium metal with the IL-LGE electrolyte, Li/Li symmetric cells using 20 μm lithium metal were constructed and compared against cells with the baseline electrolyte. The symmetric cells were cycled at a current density of 1 mA cm^{-2} with a capacity of 1 mAh cm^{-2}. Analysis of the voltage profiles reveals that cells with the IL-LGE electrolyte exhibit an initial overpotential of approximately 30 mV, which increases marginally to ~40 mV after 100 cycles. In contrast, cells with the baseline electrolyte display a higher initial overpotential of ~60 mV, followed by a continuous increase in overpotential. This leads to voltage instability (>4 V) at the 95th cycle and subsequent cell failure, indicating continuous impedance growth within the system (Fig. S11 and Section S8). The lithium plating and stripping on copper foil with IL-LGE electrolyte demonstrated an average coulombic efficiency of 99.18% over 100 cycles (Fig. S12 and Section S8).

EIS measurements were then conducted before cycling, after the first cycle, and after 100 cycles. Distribution of relaxation times (DRT) plots were generated from the EIS measurements as a complementary analysis tool to provide a more detailed qualitative impedance analysis based on the peak character of the respective time constant. DRT plots offer additional insights into the charge transfer resistance and SEI resistance as they are convoluted in Nyquist plots.[64] The equivalent circuit model used for EIS fitting (Fig. S13), along with the resulting Nyquist plots (Fig. S14a and b) and DRT plots (Fig. S14c and d), are detailed in Section S9. The bulk electrolyte diffusion resistance (R_1) remains negligible (<20 Ω) for both electrolytes, although an increasing trend is observed in both cases, likely due to electrolyte depletion in the separators over time[65] (Fig. S14e and f). In the baseline electrolyte, R_2 increases approximately fivefold (from ~100 to ~500 Ω) between the 1st and 95th cycles. Conversely, the IL-LGE electrolyte exhibits a decreasing trend in R_2 (from ~75 to ~50 Ω) over the same period. The DRT plot for the baseline electrolyte shows a notable peak shift in the first RC circuit (charge transfer), emphasizing an increase in R_2 or CPE_2 (constant phase element part of SEI) or both. The peak shift indicates growth of the electrochemical double layer and suggests higher electrolyte species depletion or non-uniform distribution near the interface.[66] In contrast, the IL-LGE electrolyte shows no significant peak shifts in the first RC circuit of the DRT plot, with a decreasing peak intensity of RC impedance, suggesting a lower electrochemical double layer growth over cycling. The SEI interfacial resistance (R_3) in the IL-LGE electrolyte also decreases (from ~60 to ~45 Ω), with only a slight increase in Warburg diffusion impedance ($W3$) (~45 Ω s$^{1/2}$ to ~52 Ω s$^{1/2}$), indicating the potential formation of a uniform, highly ionically conductive SEI. The baseline electrolyte, however, exhibits an increase in interfacial resistance (from ~580 to ~700 Ω) and a tenfold increase in Warburg impedance (from ~500 to ~5000 Ω s$^{1/2}$) from the 1st to the 95th cycle. This suggests significant growth of the SEI layer with sluggish ionic conductivity, explaining the cell failure at the 95th cycle. Further morphological and interfacial analyses of the Li metal SEI are detailed in subsequent sections.

High voltage NMC811 full cell performance with lithium metal anode

The electrochemical performance of the IL-LGE electrolyte was evaluated using a 20 μm thick Li anode and NMC811 cathode with an areal loading of ~2.6 mAh cm^{-2}. The 20 μm thick Li metal anode provides 158.6% excess capacity relative to the cathode's areal capacity. At a 4.4 V cutoff voltage, the Li-NMC full cells with IL-LGE electrolyte demonstrate 91.48% capacity retention after 150 cycles, with an average coulombic efficiency (CE) of 99.20%. In contrast, the baseline electrolyte exhibits rapid capacity fading from 50 cycles, reaching 80% capacity retention after 88 cycles, and 22.26% after 133 cycles with an average CE of 97.39% before cell failure (Fig. 4a). At a higher cutoff voltage of 4.6 V, the IL-LGE-based cells maintain 80% capacity retention after 150 cycles with an average CE of 99.47%. The baseline electrolyte, however, displays accelerated capacity fading, reaching 80% capacity retention after only 28 cycles and retaining just 27.13% after 150 cycles, with an average CE of 98.89% before cell failure (Fig. 4b). The superior electrochemical performance of the IL-LGE electrolyte results from its enhanced high-voltage stability and compatibility with lithium metal anodes. The performance metrics of the IL-LGE electrolyte are compared with other reported studies on electrolyte designs for Li‖NMC811 cells in Table S2, Fig. S15 and Section S10. While many studies employ asymmetric charge–discharge rates to enhance Li metal performance, this work utilizes symmetric charge–discharge rates, providing a more stringent evaluation of the electrolyte's capabilities (Fig. S16 and Section S10).

Low-temperature performance of the electrolytes was evaluated by both charging and discharging cells at the selected temperatures to simulate real-world battery applications. The discharge behavior of Li‖NMC811 full cells with baseline and IL-LGE electrolytes is shown in Fig. 4c over a wide temperature range. While both electrolytes exhibit similar capacity at 20 °C, the baseline cells fail completely at −40 °C and −60 °C. In contrast, the IL-LGE electrolyte retains 37.5% of its capacity at −40 °C and approximately 8% at −60 °C, representing the lowest temperature performance reported to date for IL-based electrolytes. The low viscosity of the IL-LGE electrolyte not only facilitates Li$^+$ transport at low temperatures but also enhances cathode wettability, addressing a significant limitation of conventional IL-based electrolytes.[67] Furthermore, the IL-LGE electrolyte exhibits superior rate capability compared to the baseline electrolyte at charge and discharge rates of C/3, C/2, and 1C. Lower polarization is observed at higher rates in the IL-LGE electrolyte, due to its higher 'effective Li$^+$ conductivity'.

Characterization of cycled electrolyte and interface

To investigate the interface composition and morphology of the cycled electrodes, NMC811 cathodes and Li metal anodes were collected after the first and 50th cycle with 4.4 V as the cutoff voltage. Notably, cathodes cycled for 50 cycles in the baseline electrolyte delaminate from the current collector, while those cycled in IL-LGE electrolyte remain intact (inset image of Fig. 5a and c).
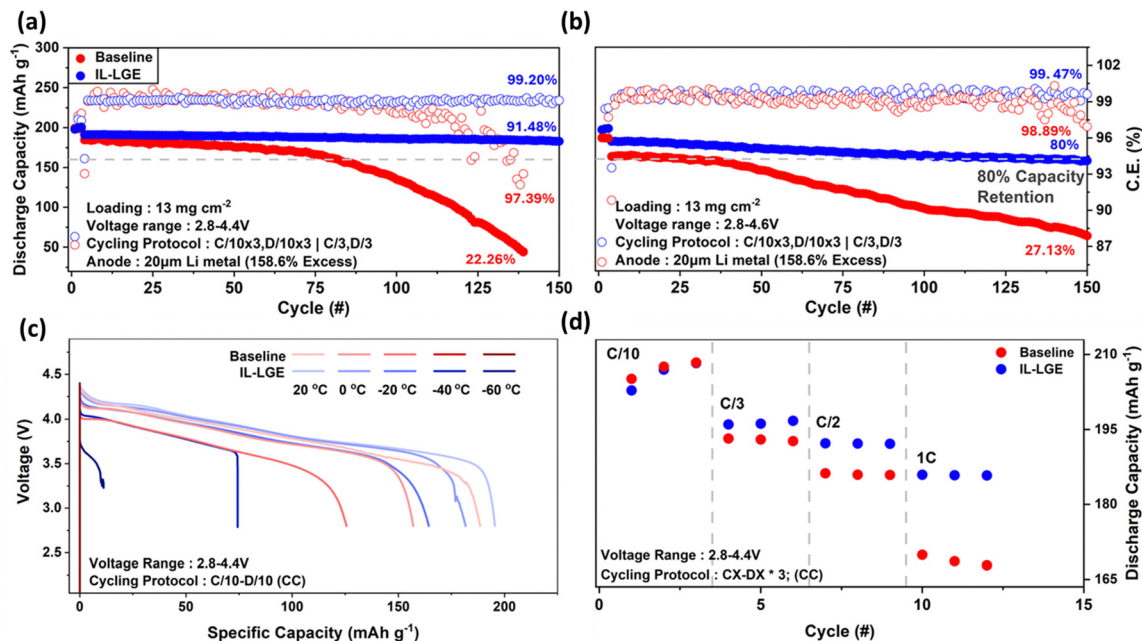
This journal is © The Royal Society of Chemistry 2025

Energy Environ. Sci., 2025, **18**, 8889–8906 | **8895**

Fig. 4   Cycling performance of IL-LGE *vs.* baseline electrolyte with a charging cutoff voltage of (a) 4.4 V and (b) 4.6 V. (c) Low temperature performance and (d) rate capability comparison of IL-LGE *vs.* baseline electrolyte.

To assess potential aluminum corrosion, a voltage hold at 4.85 V for 24 hours was conducted on both IL-LGE and baseline electrolytes, using Li metal as the counter electrode and aluminum as the working electrode. SEM images of the recovered aluminum foils reveal severe pitting in the baseline electrolyte (Fig. 5a), whereas no pitting is observed with IL-LGE (Fig. 5b).

Kühnel *et al.* investigated the impact of *N*-butyl-*N*-methyl-pyrrolidinium bis(trifluoromethanesulfonyl)imide ($Pyr_{14}TFSI$) on mitigating aluminum corrosion in LiTFSI-PC electrolyte.[68] A direct correlation between the IL concentration in the electrolyte and the suppression of aluminum corrosion was observed. This correlation was observed due to the limited
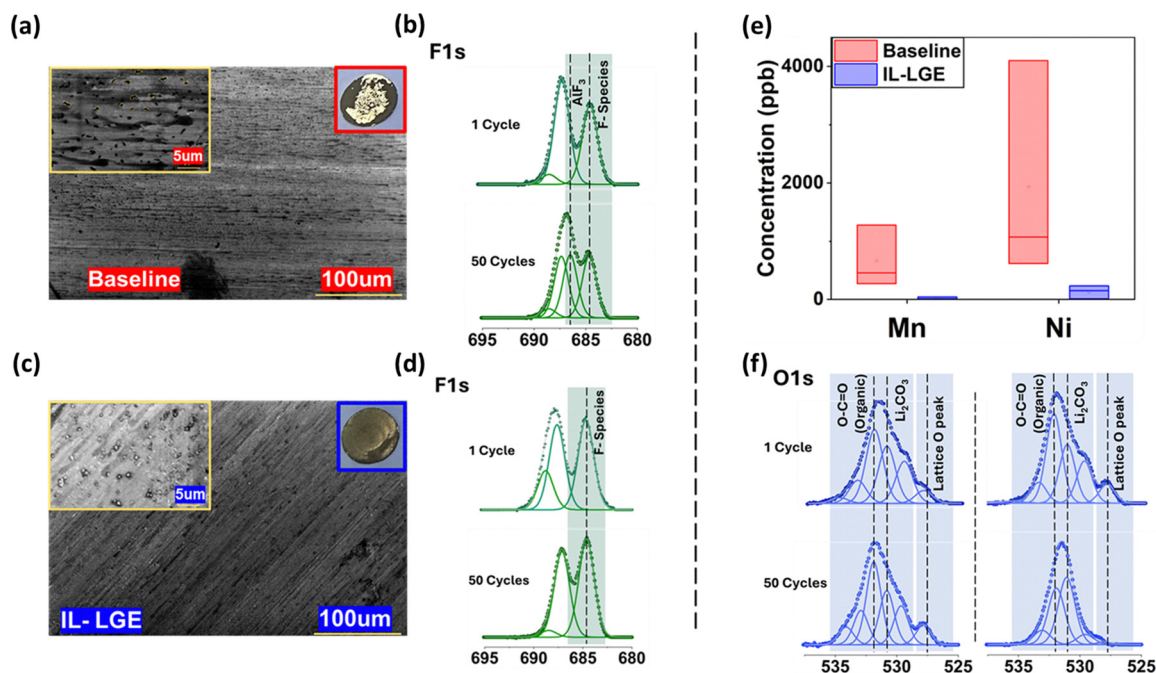
Fig. 5   (a) Aluminum current collector corrosion, delamination of cathodes in (a) baseline and (c) IL-LGE. F 1s XPS spectra of the cycled NMC811 cathode in (b) baseline and (d) IL-LGE electrolyte. (e) Concentration of Mn and Ni in cycled electrolytes *via* ICP-MS. (f) O 1s XPS spectra of cycled NMC811 cathode in baseline (left) and IL-LGE (right) electrolyte.

8896 | *Energy Environ. Sci.*, 2025, **18**, 8889–8906

This journal is © The Royal Society of Chemistry 2025

solubility of $Al(TFSI)_3$, a by-product of aluminum corrosion induced by LiTFSI. The combination of an IL as the primary solvent and FM, a low dielectric constant solvent, as a diluent in IL-LGE suppresses corrosion by reducing the solubility of $Al(TFSI)_3$.

XPS was performed on the cathode surfaces cycled for 1 and 50 cycles. The F 1s spectra of cathode surfaces cycled in both baseline (Fig. 5b) and IL-LGE (Fig. 5d) electrolytes show the presence of F^- species (~ 684.8 eV), possibly LiF. Additionally, AlF_3 is observed in the F 1s spectrum (~ 687.5 eV) of the sample cycled in the baseline electrolyte, corroborating aluminum corrosion. It has previously been reported that preferential oxidation of EC against aluminum oxide surfaces at high voltages leads to aluminum corrosion through HF generation in $LiPF_6$-based electrolyte systems.[69]

The O 1s spectra (Fig. 5f) reveal that the lattice oxygen peak of the cathode cycled in IL-LGE is nearly absent after 50 cycles, indicating the formation of a uniform, cathode–electrolyte interphase (CEI). Conversely, the strong lattice oxygen peak observed in the cathode cycled with the baseline electrolyte suggests a lack of uniform CEI formation. The formation of HF through $LiPF_6$ hydrolysis, catalyzed by H_2O generated from carbonate solvent dehydrogenation, has been identified as a key factor in non-uniform cathode–electrolyte interphase (CEI) formation in $LiPF_6$-carbonate electrolyte systems.[35] Potential dehydrogenation mechanisms were investigated using DFT calculations with $LiNiO_2$ (LNO) as a model surface. LNO is used to model a NMC cathode, eliminating concerns about metal center distribution at the surface. The thermodynamic favorability of pyrrolidinium ring dehydrogenation is demonstrated through DFT analysis of Pyr_{13}^+ on the LNO surface, resulting in O–H bond formation with a reaction energy of -0.75 eV (Fig. S17a, b and Section S11). The usage of LiTFSI salt instead of $LiPF_6$ mitigates the risk of hydrolysis reactions that could otherwise be triggered by moisture generated from Pyr_{13}^+ dehydrogenation, which is likely responsible for the preservation of the uniform CEI observed in oxygen spectra. Also, the defluorination of TFSI-ions on the LNO surface is found to be endothermic ($\Delta E = 0.29$ eV, unfavorable) (Fig. S17c, d and Section S11). This dovetails with the expectation that defluorination is generally favored under electrochemically reductive, not oxidative, conditions. A detailed XPS analysis of the cathodes is provided in the SI (Fig. S18–S20 and Section S12).

The baseline electrolyte, being in a liquid state, was directly collected following electrochemical performance testing. For the IL-LGE electrolyte, the FM was first released, and the residual $Pyr_{13}TFSI$–LiTFSI mixture was recovered using DMC solvent. The resulting solution was then diluted to a volume comparable to that of the baseline electrolyte. Inductively coupled plasma mass spectrometry (ICP-MS) analysis of the cycled electrolytes recovered after 50 cycles reveals significantly higher concentrations of Ni and Mn in the baseline electrolyte compared to the IL-LGE electrolyte (Fig. 5e). The observed trend can be attributed to two factors: the low solubility of the aggregate-rich IL-LGE electrolyte[70] and a uniform CEI in the IL-LGE system.

Cross-sectional SEM image of the cycled Li metal anode after 50 cycles indicates the presence of a thin, compact SEI in IL-LGE and a thick, porous SEI in the baseline electrolyte. These results align with the observation from the EIS of the Li/Li symmetric cell which shows a tenfold increase in the Warburg impedance indicating a very long diffusion length – a thick buildup (>34 μm) was observed in the baseline electrolyte, in contrast to IL-LGE (~ 9 μm) (Fig. S21 and Section S13).

Depth profiling XPS was employed to evaluate the evolution of SEI's chemical composition in both electrolytes. Detailed XPS spectra and elemental analyses are provided in the SI (Fig. S22 and Section S13). XPS results for the baseline electrolyte reveal a decrease in carbon content and a higher fluorine content during etching. Carbon content decreases by approximately 50% from the surface ($\sim 49\%$) to the innermost layer ($\sim 27\%$), while fluorine content is high at the surface ($\sim 16\%$) and increases to 23% in the innermost layer. Oxygen content also increases along the etching length from $\sim 33\%$ to $\sim 47.5\%$. The major components of the SEI are identified as Li_2CO_3 and LiF. Although present in lower atomic ratios (~ 1.7 to $\sim 2.4\%$), phosphorus-containing species, such as $LiPO_xF_y$, are observed to increase with etching depth. Recent studies by Steinberg et al.[71] have demonstrated the superior capability of Li_2CO_3 in enabling the formation of a highly ionic conductive interphase due to its reductive instability, leading to the co-formation of Li_2O and Li_2C_2 in a multiphasic film. However, their work also showed that in the presence of $LiPF_6$ salt, PF_6^- anions react with Li_2CO_3, forming LiF, CO_2, and F_2PO_2Li, destabilizing the microstructure of the SEI. Computational results from Spotte–Smith et al.[72] further indicated faster kinetics for the reaction of $LiPF_6$ with Li_2CO_3 in the SEI compared to moisture in the electrolyte. The observed trend of decreasing carbon content and increasing fluorine content from our XPS analysis corroborates this reaction pathway. The lower phosphorus content and reduced peak intensity of $LiPO_xF_y$ species in our XPS analysis can be attributed to the soluble nature of F_2PO_2Li species formed during these reactions. The disruption of the SEI layer and depletion of Li_2CO_3 content is expected to result in continuous growth of the SEI layer, increasing impedance and exacerbating sluggish ionic transport. These observations align with the EIS results from symmetric cells and cross-sectional images of the cycled lithium metal anodes.

In contrast to the baseline electrolyte, the IL-LGE electrolyte exhibits a relatively stable composition of carbon, oxygen, and fluorine during etching. The carbon content decreases slightly from the surface ($\sim 46\%$) to the innermost layer ($\sim 40\%$), a less pronounced reduction compared to the baseline electrolyte. The overall fluorine content at the surface is lower than in baseline electrolyte ($\sim 9.5\%$) and remains relatively stable in the innermost layer (11%). Oxygen content increases moderately along the etching length from the surface (from ~ 43 to $\sim 47\%$). The dominant species in the IL-LGE electrolyte are found to be Li_2CO_3 and LiF. Although present in lower atomic ratios (from ~ 1.29 to $\sim 2.25\%$), sulphur-containing species, such as Li_2S, are observed to increase with etching depth. The lower abundance of sulfur-containing species in the SEI

suggests that the interfacial products are predominantly derived from the decomposition of FM and CO_2, rather than from the $TFSI^-$ anions. The relatively stable trend in carbon and fluorine composition during etching indicates preservation of Li_2CO_3, which is expected to lead to a highly ionic conductive multiphasic film of Li_2O and Li_2C_2. This observation is further supported by the decrease in SEI resistance (R_3) observed in the EIS analysis of Li/Li symmetric cells from the 1st to the 100th cycle. The formation and preservation of the Li_2CO_3 component on the Li metal surface appears to be crucial for the enhanced performance of Li metal batteries in the IL-LGE electrolyte system. Liu et al.[73] reported Pyr_{13}^+ to be more corrosive to the Li metal anode than $EMIM^+$ due to its lower nitrogen content. Using radial distribution curves, Liu et al.[74] examined IL cation coordination with electrolyte species to study the cation's interaction with electrolyte components. Similar analysis is conducted for the formulated IL-LGE ($LiTFSI : Pyr_{13}TFSI : FM$ – $1 : 0.7 : 15$), revealing Pyr_{13}^+ as being completely solvated by FM molecules in the first solvation sheath, due to the absence of free $TFSI^-$ in the formulated electrolyte. The solvation of Pyr_{13}^+ by FM is evident from the radial distribution plot showing a peak of Pyr_{13}^+ coordination with FM (F) at ~ 4.3 Å (Fig. S22 and Section S13). The FM shielding of Pyr_{13}^+ suppresses Pyr_{13}^+ decomposition, as evidenced by the near ~ 0 atomic wt% of nitrogen-derived components (Fig. S23 and Section S13). The SEI were found to be predominantly CO_2, FM and $TFSI^-$ derived rather than Pyr_{13}^+ derived.

To further validate the unique role of FM in enabling aggregate-rich solvation structures, we conducted comparative studies using 1,1,2,2-tetrafluoroethyl 2,2,3,3-tetrafluoropropyl ether (TTE) as an alternative co-solvent analogue. Although high concentrations of LiTFSI in $Pyr_{14}TFSI$ have been reported for polymer-based electrolytes,[75] we selected TTE as a liquid co-solvent to investigate the role of FM diluents in the system, given that TTE has been previously demonstrated as a suitable diluent for IL-based electrolytes.[76] While TTE required higher

IL concentrations ($LiTFSI : Pyr_{13}TFSI$ molar ratios up to $1 : 2.0$) to achieve miscibility, Raman spectroscopy revealed that TTE-based electrolytes retained prominent free $TFSI^-$ signatures, unlike FM-based systems (Fig. S24, S25 and Section S14). Electrochemical testing showed that the IL-TTE electrolyte failed immediately in Li/Li symmetric cells due to extreme overpotentials, whereas low-concentration IL-LGE ($LiTFSI : Pyr_{13}TFSI : FM$ molar ratio of $1 : 2.0 : 15$) exhibited progressively increasing impedance and failed after 20 cycles (Fig. S26, S27 and Section S14). In contrast, high-concentration IL-LGE ($LiTFSI : Pyr_{13}TFSI : FM$ molar ratio of $1 : 0.7 : 15$) maintained stable cycling performances. Full-cell testing with NMC811 cathodes confirmed these trends: TTE-based electrolytes failed during initial cycling, while FM-based systems demonstrated stable operation (Fig. S28, S29 and Section S14). Post-mortem analysis using XPS and FIB-SEM revealed extensive SEI buildup (> 34 μm) and electrolyte decomposition in systems containing free $TFSI^-$, confirming the critical importance of FM's ability to eliminate free $TFSI^-$ species while maintaining aggregate solvation structures for stable lithium metal operation (Fig. S30–S32 and Section S14).

Based on these findings, the mechanistic understanding for the improved cycling performance of the IL-LGE electrolyte compared to the baseline electrolyte in 20 μm Li∥NMC811 full cells is summarized in Fig. 6. In the baseline electrolyte, PF_6^- anions react with the Li_2CO_3 component of the SEI, formed by carbonate decomposition, resulting in disruption and destabilization of the SEI layer while forming LiF and soluble $LiPO_xF_y$ species. This leads to a matrix with sluggish ionic conductivity, inducing significant cell impedance. On the cathode side of the baseline system, carbonates are prone to oxidation on the Al_2O_3 layer of the current collector, forming H_2O. This H_2O subsequently reacts with PF_6^- anions to produce corrosive HF, potentially causing cathode delamination during long-term cycling.[35,48]

Further decomposition of carbonates on the cathode surface releases additional H_2O, perpetuating HF formation and
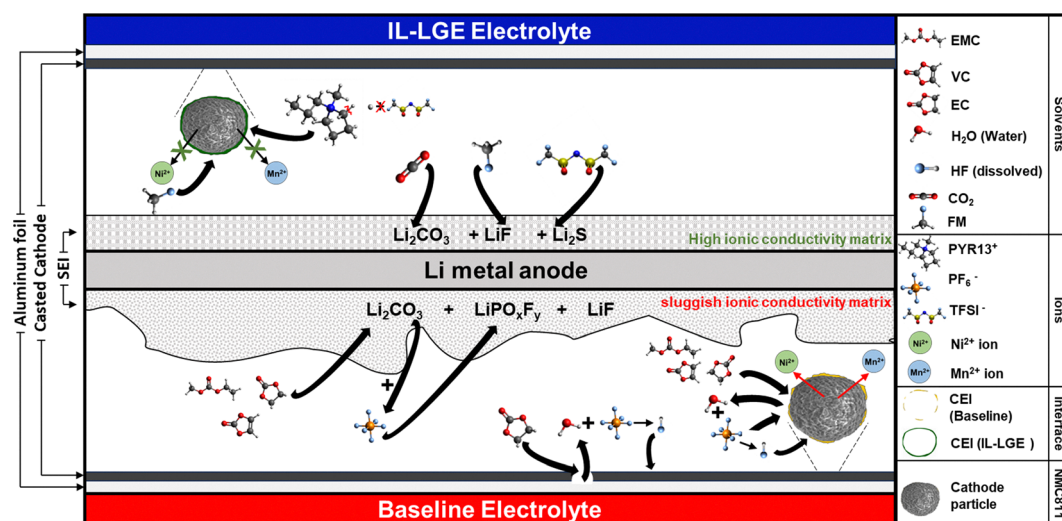

Fig. 6   Schematics of the performance improvement by IL–LGE electrolyte over the baseline electrolyte in the NMC811/20 μm Li full cell.

potentially degrading the cathode surface and CEI, leading to increased transition metal dissolution in the electrolyte. In contrast, the IL-LGE system preserves the Li_2CO_3 in the SEI, formed by CO_2 reduction, enabling a highly conductive SEI matrix. This matrix also includes LiF and Li_2S formed through decomposition of FM and $TFSI^-$, as well as reduction products of the pyrrolidinium backbone, collectively reducing overall cell impedance. On the cathode side, a uniform CEI layer is observed after extended cycling, forming a passivating interphase. Minimal to negligible transition metal dissolution is observed, due to the low solubility of the aggregate-rich electrolyte design and the formation of a uniform CEI, collectively enhancing the cathode stability. The IL-LGE demonstrates enhanced stability towards both the Li metal anode and high-nickel NMC811 cathode material, enabling superior performance in high-voltage Li metal batteries.

Solvent and ionic liquid recovery from IL-LGE

While establishing a circular economy in energy storage systems is crucial for reducing costs and mitigating environmental impacts associated with improper battery disposal, developing more sustainable and environmentally friendly methods to achieve this goal remains a significant challenge.[77] Conventionally, supercritical CO_2 is employed for electrolyte extraction from both separators and electrode materials. However, the handling of supercritical CO_2 presents a significant challenge in scaling up the recycling process.[78] Given the gaseous nature of LGE based systems, the recovery of liquefied gas solvents is comparatively more straightforward than that of widely used liquid organic solvents.

Previous work by Y. Yijie *et al.* demonstrated the recycling of LGE solvents, recovering a gaseous mixture of Me_2O and TFE from spent electrolyte for use in new batches of electrolytes. While this recovery process represents a significant step towards enabling a circular economy, its application is limited by the recovery of solvents as a mixture rather than as individual components.[28] ILs are commonly referred to as 'green solvents' due to their exceptionally low volatility and high thermal stability.[79] Numerous studies have reported the use of ILs in flue gas recovery, made possible by the ability to recover these ILs without decomposition.[80–82] $Pyr_{13}TFSI$, the IL employed in this work, also exhibits exceptional thermal stability and low volatility,[83] making its recovery from the electrolyte feasible.

In this work, we present a conceptual demonstration of the recovery of individual electrolyte components, adding a new dimension to the circular economy of energy storage systems.
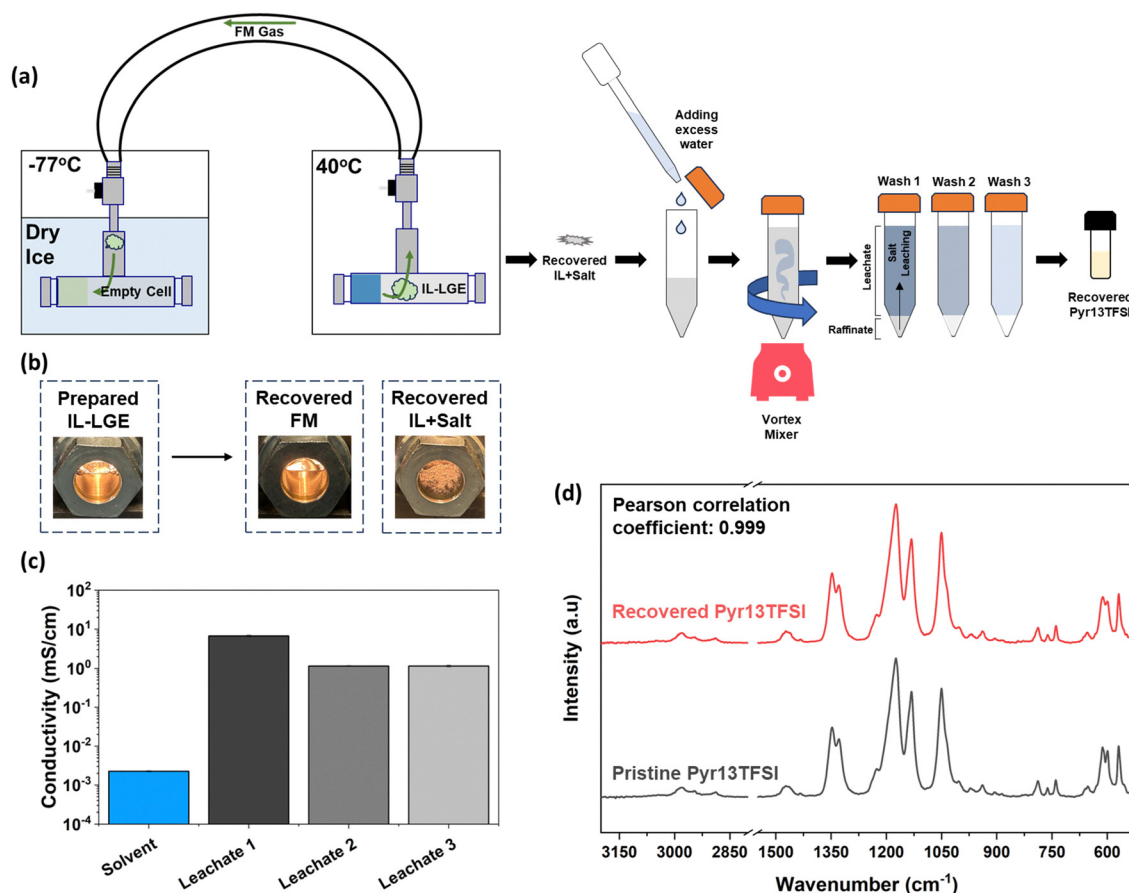

Fig. 7 (a) Workflow of the co-solvent and ionic liquid recovery process. (b) Window cells of the prepared IL-LGE electrolyte and recovered FM solvent and IL + salt mixture. (c) Conductivity plot of the solvent used and the leachates obtained after the washes. (d) IR spectrum comparison of recovered and pristine Pyr13TFSI ionic liquid.

This journal is © The Royal Society of Chemistry 2025

Energy Environ. Sci., 2025, **18**, 8889–8906 | **8899**

The recovery workflow is depicted in Fig. 7a. The initial step involves recovering the gaseous component (FM) from the IL-LGE electrolyte by exploiting the relationship between vapor pressure and temperature. The process involves connecting an empty cell to the cell with IL-LGE. The empty cell is cooled to -77 °C, while the electrolyte cell is maintained at ~ 40 °C, near the critical temperature (T_c) of FM (T_c = 44.8 °C). Upon opening the cell with IL-LGE, the FM gas rapidly transfers to the cooled cell due to the pressure difference induced by the temperature gradient, where it liquefies. This process leaves behind an IL and salt residue with minimal to no FM, attributable to FM's limited participation in the solvation structure and its lack of vapor pressure depression ($P_{\text{IL\_LGE}}$ cell = $P_{\text{v.p of FM}}$), enabling complete FM transfer. Fig. 7b displays the recovered liquefied FM and the IL + salt residue. Mass measurements of the cells before and after the transfer process indicate no significant loss of FM during the transfer (Fig. S33 and Section S15).

Following the recovery of the IL + salt residue, a leaching technique was employed to extract the LiTFSI salt from the IL. Distilled water was selected as the leaching solvent due to the high solubility of LiTFSI in water (>21 M)[84] and the hydrophobic nature of Pyr$_{13}$TFSI.[85] Both the LiTFSI salt and Pyr$_{13}$TFSI IL demonstrate chemical stability in water. The use of water as a leaching agent further validates the process's sustainability due to its economic viability and non-toxic nature.[86] Excess water was added to the IL + salt mixture in a centrifuge tube and subjected to mixing via a vortex mixer to ensure maximum salt leaching. After mixing, the solution was left to rest overnight, and the leachate that accumulated in the top portion of the phase-separated solution was recovered. Leachate conductivity was measured to ensure salt leaching and estimate the number of washes required (Fig. 7c). Ideally, the leachate conductivity should approach that of the leaching solvent once all salt is extracted. However, leaching was terminated after conductivity values remained constant for leachates 2 and 3—despite being two orders of magnitude higher than expected—due to the observation of floating IL particles in the leachate solution, which potentially increased conductivity.

After three washes, the remaining raffinate was recovered and heated in a vacuum oven at 120 °C overnight to remove residual moisture. The recovered raffinate was analyzed using infrared (IR) spectroscopy and found to closely match the spectrum of pristine Pyr$_{13}$TFSI (Fig. 7d). FTIR is a widely employed analytical technique for verifying compound purity and is also employed in assessing the purity of ILs, as it allows for direct comparison of spectral features between the sample of interest and a known pure reference.[87,88] IR spectra were also collected and compared for the LiTFSI salt, recovered IL + salt residue, and a prepared IL + salt mixture with the optimized IL + salt molar ratio for IL-LGE formulation (Fig. S34 and Section S15). Analysis showed no detectable LiTFSI in the recovered IL, confirming its purity (Pearson correlation coefficient = 0.999). The yield of the IL was not considered due to observed losses in leachates, as this demonstration is conceptual in nature. The recovered leachates can potentially be dehydrated to recover LiTFSI salt, provided they are free of IL

content. This proposed technique not only demonstrates the recovery workflow of electrolyte components but also highlights the recoverability of the IL-LGE electrolyte design.

While FM does not directly improve salt recovery, it facilitates easier separation of co-solvents compared to other liquid co-solvents. To support this, the LiTFSI/Pyr$_{13}$TFSI + TTE (IL-TTE) electrolyte was recovered from the failed cell in Fig. S35 and Section S15, where LiTFSI was leached out using DI water. The raffinate, clearly phase-separated from excess water (Fig. S35a and Section S15), was identified via FTIR as a mixture of Pyr$_{13}$TFSI and TTE. Although the characteristic –SO$_2$ (1329 cm^{-1}) and –CF$_3$ (329 cm^{-1}) modes of Pyr$_{13}$TFSI (red arrows) are visible, they are largely masked by the C–O–C ether stretching ($\sim$1100 cm^{-1}) of TTE (blue arrows) as seen in Fig. S35b and Section S15. In contrast, the raffinate from the FM-based IL-LGE more closely matches pristine Pyr$_{13}$TFSI in its FTIR spectrum. Thus, FM appears to simplify the co-solvent separation step during electrolyte recovery. In comparison, separating traditional liquid co-solvents (e.g., IL and TTE) typically requires distillation or liquid–liquid separation, which can be significantly more costly and complex at scale.

Conclusions

This study presents the development and evaluation of an aggregate-rich liquefied gas electrolyte based on ionic liquids. Despite the presence of aggregate-rich solvation structures, the participation of FM in the solvation structure enabled high 'effective Li$^+$ conductivity', achieving one of the highest reported Li$^+$ conductivities for ionic liquid-based electrolytes (17.7 mS cm^{-1}) and the lowest operability temperature (-60 °C) for Li-based ionic liquid electrolytes to date. The IL-LGE electrolyte was observed to preserve Li$_2$CO$_3$ in the SEI layer of the Li metal anode, enabling a stable lithium metal anode with a highly conductive SEI matrix, in contrast to the baseline electrolyte. A uniform CEI layer, facilitated by the electrolyte design and the low solubility of the aggregate-rich electrolyte, was found to inhibit transition metal dissolution, thereby stabilizing the cathode. These design features and observations translated into superior electrochemical performance in 20 μm Li‖NMC811 batteries at cutoff voltages of 4.4 and 4.6 V. The system demonstrates a capacity retention of 91.8% at 4.4 V and 80% at 4.6 V after 150 cycles, while maintaining operability down to -60 °C. Additionally, the recoverability properties of liquefied gas solvents and ionic liquids were exploited to establish a conceptual workflow for electrolyte component recovery, demonstrating the recovery of high-purity ionic liquid. This work highlights the potential of exploiting the complementary nature of ionic liquids and liquefied gas solvents in advancing the development of next-generation energy storage systems.

Materials and method

Materials

The salts lithium bis(fluorosulfonyl)imide (LiFSI) (99.9%) and lithium bis(trifluoromethane)sulfonimide (LiTFSI) ($>$99.5%),

8900 | *Energy Environ. Sci.*, 2025, **18**, 8889–8906

This journal is © The Royal Society of Chemistry 2025

and solvent 1,1,2,2-tetrafluoroethyl 2,2,3,3-tetrafluoropropyl ether (TTE) were obtained from Sigma Aldrich. Fluoromethane (99.99%) and carbon dioxide (99.99%) were purchased from commercial sources. 1.2 M LiPF$_6$ (lithium hexafluorophosphate) in EC (ethylene carbonate)/EMC (ethyl methyl carbonate) 3:7 (wt:wt) + 2 wt% VC (vinylidene carbonate) baseline was obtained from Sandia National Laboratories. The ionic liquids *N*-methyl-*N*-propyl-pyrrolidinium bis(trifluoromethane)sulfonimide and *N*-methyl-*N*-propyl-pyrrolidinium bis(fluorosulfonyl)imide were purchased from ROCO Global. The LiNi$_{0.8}$Mn$_{0.1}$Co$_{0.1}$O$_2$ (NMC811) material was obtained from Pacific Northwest National Laboratory (Fig. S1 and Section S1). The 20 μm Lithium metal foil was provided by Elevated Materials Inc.

Electrode preparation

To evaluate the electrochemical performance of IL-LGE and baseline electrolytes, NMC811 cathodes were prepared using SPC65 (carbon black, TIMCAL Ltd) as the conductive agent and HSV900 (PVDF, Arkema Inc.) as the binder, in a mass ratio of 96:2:2. The cathode loading was around 2.6 mAh cm^{-2}. The components were mixed with 50 wt% of *N*-methyl-2-pyrrolidone (NMP, ≥99%, Sigma-Aldrich) in a Thinky Mixer to form a homogeneous slurry. This slurry was cast onto aluminum foil and dried overnight at 80 °C in a vacuum oven, followed by an additional drying step at an elevated temperature of 120 °C for one hour. The resulting cathode film was punched into discs with a diameter of 1/4 inch, yielding an active mass loading of approximately 13 mg cm^{-2}.

Cryogenic focused ion beam scanning electron microscopy (Cryo-FIB-SEM)

FIB-SEM was conducted on the FEI Scios Dual-beam microscope. Discharged cells were disassembled in an Ar-filled glovebox after cycling and the samples were transferred to the microscope chamber *via* an airtight loader. The electron beam operated at 5 kV, and the sample stage was cooled to −180 °C with liquid nitrogen. Sample cross-sections were exposed using a 1 nA ion beam current and cleaned at 0.1 nA.

Electrolyte screening

The solvents chosen for electrolyte screening include: ionic liquids—[BMIM][TFSI] (1-butyl-3-methylimidazolium bis(trifluoromethylsulfonyl)imide), [EMIM][TFSI] (1-ethyl-3-methylimidazolium bis(trifluoromethylsulfonyl)imide), [BMIM][BF$_4$] (1-butyl-3-methylimidazolium tetrafluoroborate), [EMIM][BF$_4$] (1-ethyl-3-methylimidazolium tetrafluoroborate), [BMIM][PF$_6$] (1-butyl-3-methylimidazolium hexafluorophosphate), [EMIM][PF$_6$] (1-ethyl-3-methylimidazolium hexafluorophosphate), [Pyr$_{13}$][FSI] (*N*-methyl-*N*-propylpyrrolidinium bis(fluorosulfonyl)imide), [Pyr$_{13}$][TFSI] (*N*-methyl-*N*-propylpyrrolidinium bis(trifluoromethylsulfonyl)imide); organic solvents—DME (1,2-dimethoxyethane), DfbN (difluorobenzene), EC (ethylene carbonate), EMC (ethyl methyl carbonate), PC (propylene carbonate); liquefied gas solvents—Me$_2$O (dimethyl ether), DFM (difluoromethane), TFE (1,1,1,2-tetrafluoroethane), FM (fluoromethane).

X-ray photoelectron spectroscopy (XPS)

X-ray photoelectron spectroscopy (XPS) samples were prepared by electrochemical cycling of 20 μm Li‖NMC811 cells. The cycled NMC811 samples were gently rinsed with dimethyl carbonate (DMC), while the cycled 20 μm Li samples were rinsed with 1,2-dimethoxyethane (DME) in an Ar-filled glovebox to remove residual Li salts. Both sample types were subsequently dried in the glovebox antechamber. To prevent exposure to moisture and air, the samples were sealed and transferred directly to the XPS instrument chamber.

Cathode surface. XPS measurements were taken on a Kratos AXIS Supra (Sandia National Laboratory) operated at a base pressure better than 5×10^{-9} Torr, using a monochromatic Al Kα X-ray source (λ = 1486.6 eV). Surveys and high-resolution spectra for elements of interest were taken on each sample. Spectra were obtained using a large analyzer spot size and a pass energy of 160 eV for all surveys and 20 eV for the high-resolution elements, with a step size of 0.1 eV for F 1s, O 1s, C 1s, P 2p, and Li 1s, and 0.07 eV for all other elements. Charge compensation was done using a charge neutralizer with a filament current of 0.42 A.

Anode surface. XPS measurements were performed on a Kratos AXIS Supra DLD instrument (UC Irvine) with monochromatized Al Kα radiation (λ = 0.83 nm and $h\nu$ = 1486.7 eV) under a base pressure of $<10^{-8}$ Pa. Depth profiling of Li metal was performed using an Ar$_{500}^+$ cluster ion beam at 5 keV, with etching times of 60 s, 120 s, and 300 s.

CasaXPS software was employed for spectral analysis, with all spectra calibrated to the F 1s peak of F-species and the C 1s peak (284.6 eV).

Raman spectroscopy

A Renishaw inVia confocal Raman microscope was used to acquire the Raman spectra of the LGEs, employing a green laser with an excitation wavelength of 532 nm. Silicon (520 nm) was used to calibrate all spectra, and subsequent analysis was performed using WiRE 3.4 software developed by Renishaw Ltd.

Electrochemical tests

Electrolyte conductivity was measured using a custom-fabricated high-pressure stainless steel (SS) cell setup, employing polished SS (316L grade) electrodes. The cell constant was calibrated using OAKTON standard conductivity solutions (0.447–80 mS cm^{-1}). The Li$^+$ transference number in the electrolyte was determined using a potentiostatic polarization method with an applied voltage of 5 mV. The cell configuration consisted of two Li–metal foils sandwiched between five 2500 Celgard separators.

Electrochemical impedance spectroscopy (EIS) data were collected using a Biologic SAS (SP-200) system, with ZView software utilized for spectral fitting. EIS measurements were conducted with an applied AC potential of 10 mV over a frequency range of 1 MHz to 0.01 Hz. The EIS measurements in all cases were performed on the same cell setup.

Battery cycling was conducted using customized high-pressure SS (316L) cells on an Arbin battery test station cycler

(BT2043). The full cell configuration included a 20 μm Li metal anode (5/16 inch diameter, Applied Materials), slurry casted $LiNi_{0.8}Mn_{0.1}Co_{0.1}O_2$ (NMC811) as the cathode, and a single 25 μm porous polypropylene separator (Celgard 2075). Stainless spacers and nickel foam (3/8 inch diameter) were employed as substitutes for the spacer and spring typically used in coin cells. The cell design is detailed in Section S2. All electrochemical tests used flooded electrolytes exceeding 50 g Ah^{-1}. The initial stacking pressure ranged from 200 to 400 kPa and testing was performed at an average temperature of 23 °C without specific temperature control.

For temperature-dependent studies, cells were equilibrated at the designated test temperature in an environmental chamber (Espec) for several hours prior to cycling. In Li-NMC cycling experiments, cells were subjected to two activation cycles at a C/10 rate at room temperature followed by cycling at the selected rate and temperature.

MD simulations

MD simulations were performed using many-body polarizable force field APPLE&P[31] for LiTFSI, Pyr_{13}TFSI and FM. The simulation box comprised of 1890 FM, 76 Pyr_{13}TFSI and 107 LiTFSI. A complete set of force field parameters, connectivity files and MD simulation code are provided as an archive file in the SI while a description of the files is provided in previous studies.[26,32] Initial MD simulations were performed in NPT ensemble at the pressures matching experiments, followed by production runs in NVT ensemble as summarized in Table S2.

Simulations were performed in constant volume–temperature (NVT) ensemble using Nosé–Hoover thermostat. Multiple timestep integration was employed with a timestep of 0.5 fs for bonded interactions, time step of 1.5 fs for all non-bonded interactions within a truncation distance of 7.0 Å and an outer timestep of 3.0 fs for all non-bonded interactions between 7.0 Å and the nonbonded truncation distance of 12 Å, because the heterogeneous structure of electrolyte with large ionic aggregates was surrounded by the relatively low-density solvent. The Ewald summation method was used for the electrostatic interactions between permanent charges with permanent charges or induced dipole moments with $k = 8^3$ vectors. The reciprocal part of Ewald was calculated every 3.0 fs. Induced dipoles were found self-consistently. Ion self-diffusion coefficients, inverse van Hove ratio (ionicity), self- and distinct contributions to conductivity matrix and viscosity were extracted following previously published methodology[33] and are given in Table S2.

Author contributions

G. R., M. Z., and Y. S. M. conceived the ideas. G. R., and A. L. designed the experiments together and performed the experiments. The force field was developed by O. B., who also carried out the MD simulations. K. L. carried out the DFT calculations of the ionic liquid cation on the LNO surface. N. H. provided the baseline electrolyte and collected XPS data of the cathode. M. L. collected the XPS data of the anode. N. P. performed the ICP-MS analysis. T. J. performed the detailed EIS and DRT analysis. A. L. assisted G. R. with control experiments and data processing. All authors discussed the results and commented on the manuscript.

Conflicts of interest

All authors declare no financial or non-financial competing interests.

Data availability

All the data generated in this study are included in the Article and its SI. See DOI: https://doi.org/10.1039/d5ee02265g

Raw files or additional data relevant to the paper are available from the corresponding author upon reasonable request.

Acknowledgements

of the U.S. Department of Energy or the United States Government.

References

1 H. Hesse, M. Schimpe, D. Kucevic and A. Jossen, Lithium-Ion Battery Storage for the Grid—A Review of Stationary Battery Storage System Design Tailored for Applications in Modern Power Grids, *Energies*, 2017, **10**, 2107.

2 K. M. Abraham, J. L. Goldman and D. L. Natwig, Characterization of Ether Electrolytes for Rechargeable Lithium Cells, *J. Electrochem. Soc.*, 1982, **129**, 2404–2409.

3 X. Ren, L. Zou, X. Cao, M. H. Engelhard, W. Liu, S. D. Burton, H. Lee, C. Niu, B. E. Matthews, Z. Zhu, C. Wang, B. W. Arey, J. Xiao, J. Liu, J.-G. Zhang and W. Xu, Enabling High-Voltage Lithium-Metal Batteries under Practical Conditions, *Joule*, 2019, **3**, 1662–1676.

4 S. Jiao, X. Ren, R. Cao, M. H. Engelhard, Y. Liu, D. Hu, D. Mei, J. Zheng, W. Zhao, Q. Li, N. Liu, B. D. Adams, C. Ma, J. Liu, J.-G. Zhang and W. Xu, Stable cycling of high-voltage lithium metal batteries in ether electrolytes, *Nat. Energy*, 2018, **3**, 739–746.

5 X. Fan, L. Chen, O. Borodin, X. Ji, J. Chen, S. Hou, T. Deng, J. Zheng, C. Yang, S.-C. Liou, K. Amine, K. Xu and C. Wang, Non-flammable electrolyte enables Li-metal batteries with aggressive cathode chemistries, *Nat. Nanotechnol.*, 2018, **13**, 715–722.

6 T. Li, X.-Q. Zhang, P. Shi and Q. Zhang, Fluorinated Solid-Electrolyte Interphase in High-Voltage Lithium Metal Batteries, *Joule*, 2019, **3**, 2647–2661.

7 X. Fan, X. Ji, F. Han, J. Yue, J. Chen, L. Chen, T. Deng, J. Jiang and C. Wang, Fluorinated solid electrolyte interphase enables highly reversible solid-state Li metal battery, *Sci. Adv.*, 2018, **4**(12), DOI: **10.1126/sciadv.aau9245**.

8 L. Suo, W. Xue, M. Gobet, S. G. Greenbaum, C. Wang, Y. Chen, W. Yang, Y. Li and J. Li, Fluorine-donating electrolytes enable highly reversible 5-V-class Li metal batteries, *Proc. Natl. Acad. Sci. U. S. A.*, 2018, **115**, 1156–1161.

9 T. Deng, X. Fan, L. Cao, J. Chen, S. Hou, X. Ji, L. Chen, S. Li, X. Zhou, E. Hu, D. Su, X.-Q. Yang and C. Wang, Designing *In Situ*-Formed Interphases Enables Highly Reversible Cobalt-Free LiNiO2 Cathode for Li-ion and Li-metal Batteries, *Joule*, 2019, **3**, 2550–2564.

10 M. Mao, X. Ji, Q. Wang, Z. Lin, M. Li, T. Liu, C. Wang, Y.-S. Hu, H. Li, X. Huang, L. Chen and L. Suo, Anion-enrichment interface enables high-voltage anode-free lithium metal batteries, *Nat. Commun.*, 2023, **14**, 1082.

11 Y. Yamada, J. Wang, S. Ko, E. Watanabe and A. Yamada, Advances and issues in developing salt-concentrated battery electrolytes, *Nat. Energy*, 2019, **4**, 269–280.

12 X. Cao, H. Jia, W. Xu and J.-G. Zhang, Review—Localized High-Concentration Electrolytes for Lithium Batteries, *J. Electrochem. Soc.*, 2021, **168**, 010522.

13 S. Yuan, K. Ding, X. Zeng, D. Bin, Y. Zhang, P. Dong and Y. Wang, Advanced Nonflammable Organic Electrolyte Promises Safer Li-Metal Batteries: From Solvation Structure Perspectives, *Adv. Mater.*, 2023, **35**(13), DOI: **10.1002/adma.202206228**.

14 R. Zhang, X. Shi, O. C. Esan and L. An, Organic Electrolytes Recycling From Spent Lithium-Ion Batteries, *Global Challenges*, 2022, **6**(12), 2200050.

15 J. Diekmann, C. Hanisch, L. Froböse, G. Schälicke, T. Loellhoeffel, A.-S. Fölster and A. Kwade, Ecological Recycling of Lithium-Ion Batteries from Electric Vehicles with Focus on Mechanical Processes, *J. Electrochem. Soc.*, 2017, **164**, A6184–A6191.

16 N. P. Lebedeva, F. Di Persio, T. Kosmidou, D. Dams, A. Pfrang, A. Kersys and L. Boon-Brett, Amount of Free Liquid Electrolyte in Commercial Large Format Prismatic Li-Ion Battery Cells, *J. Electrochem. Soc.*, 2019, **166**, A779–A786.

17 U. Pal, D. Rakov, B. Lu, B. Sayahpour, F. Chen, B. Roy, D. R. MacFarlane, M. Armand, P. C. Howlett, Y. S. Meng and M. Forsyth, Interphase control for high performance lithium metal batteries using ether aided ionic liquid electrolyte, *Energy Environ. Sci.*, 2022, **15**, 1907–1919.

18 M. Moreno, E. Simonetti, G. B. Appetecchi, M. Carewska, M. Montanino, G.-T. Kim, N. Loeffler and S. Passerini, Ionic Liquid Electrolytes for Safer Lithium Batteries, *J. Electrochem. Soc.*, 2017, **164**, A6026–A6031.

19 S. P. F. Costa, A. M. O. Azevedo, P. C. A. G. Pinto and M. L. M. F. S. Saraiva, Environmental Impact of Ionic Liquids: Recent Advances in (Eco)toxicology and (Bio)degradability, *ChemSusChem*, 2017, **10**, 2321–2347.

20 A. Lewandowski and A. Świderska-Mocek, Ionic liquids as electrolytes for Li-ion batteries—An overview of electrochemical studies, *J. Power Sources*, 2009, **194**, 601–609.

21 A. Fernicola, F. Croce, B. Scrosati, T. Watanabe and H. Ohno, LiTFSI-BEPyTFSI as an improved ionic liquid electrolyte for rechargeable lithium batteries, *J. Power Sources*, 2007, **174**, 342–348.

22 K. Hayamizu, Y. Aihara, H. Nakagawa, T. Nukuda and W. S. Price, Ionic Conduction and Ion Diffusion in Binary Room-Temperature Ionic Liquids Composed of [emim][BF_4] and $LiBF_4$, *J. Phys. Chem. B*, 2004, **108**, 19527–19532.

23 X. Liu, A. Mariani, H. Adenusi and S. Passerini, Locally Concentrated Ionic Liquid Electrolytes for Lithium-Metal Batteries, *Angew. Chem., Int. Ed.*, 2023, **62**(17), DOI: **10.1002/anie.202219318**.

24 X. Liu, A. Mariani, T. Diemant, M. E. Di Pietro, X. Dong, M. Kuenzel, A. Mele and S. Passerini, Difluorobenzene-Based Locally Concentrated Ionic Liquid Electrolyte Enabling Stable Cycling of Lithium Metal Batteries with Nickel-Rich Cathode, *Adv. Energy Mater.*, 2022, **12**(25), DOI: **10.1002/aenm.202200862**.

25 C. S. Rustomji, Y. Yang, T. K. Kim, J. Mac, Y. J. Kim, E. Caldwell, H. Chung and Y. S. Meng, Liquefied gas electrolytes for electrochemical energy storage devices, *Science*, 2017, **356**(6345), DOI: **10.1126/science.aal4263**.

26 Y. Yang, Y. Yin, D. M. Davies, M. Zhang, M. Mayer, Y. Zhang, E. S. Sablina, S. Wang, J. Z. Lee, O. Borodin, C. S. Rustomji and Y. S. Meng, Liquefied gas electrolytes for wide-

temperature lithium metal batteries, *Energy Environ. Sci.*, 2020, **13**, 2209–2219.

27 D. M. Davies, Y. Yang, E. S. Sablina, Y. Yin, M. Mayer, Y. Zhang, M. Olguin, J. Z. Lee, B. Lu, D. Damien, O. Borodin, C. S. Rustomji and Y. S. Meng, A Safer, Wide-Temperature Liquefied Gas Electrolyte Based on Difluoromethane, *J. Power Sources*, 2021, **493**, 229668.

28 Y. Yin, Y. Yang, D. Cheng, M. Mayer, J. Holoubek, W. Li, G. Raghavendran, A. Liu, B. Lu, D. M. Davies, Z. Chen, O. Borodin and Y. S. Meng, Fire-extinguishing, recyclable liquefied gas electrolytes for temperature-resilient lithium-metal batteries, *Nat. Energy*, 2022, **7**, 548–559.

29 S. Y. Wee and A. Z. Aris, Environmental impacts, exposure pathways, and health effects of PFOA and PFOS, *Ecotoxicol. Environ. Saf.*, 2023, **267**, 115663.

30 R. Jung, F. Linsenmann, R. Thomas, J. Wandt, S. Solchenbach, F. Maglia, C. Stinner, M. Tromp and H. A. Gasteiger, Nickel, Manganese, and Cobalt Dissolution from Ni-Rich NMC and Their Effects on NMC622-Graphite Cells, *J. Electrochem. Soc.*, 2019, **166**, A378–A389.

31 O. Borodin, Polarizable Force Field Development and Molecular Dynamics Simulations of Ionic Liquids, *J. Phys. Chem. B*, 2009, **113**, 11463–11478.

32 O. Borodin, G. A. Giffin, A. Moretti, J. B. Haskins, J. W. Lawson, W. A. Henderson and S. Passerini, Insights into the Structure and Transport of the Lithium, Sodium, Magnesium, and Zinc Bis(trifluoromethansulfonyl)imide Salts in Ionic Liquids, *J. Phys. Chem. C*, 2018, **122**, 20108–20121.

33 O. Borodin and G. D. Smith, Quantum Chemistry and Molecular Dynamics Simulation Study of Dimethyl Carbonate: Ethylene Carbonate Electrolytes Doped with $LiPF_6$, *J. Phys. Chem. B*, 2009, **113**, 1763–1776.

34 Y. Zhang, Y. Katayama, R. Tatara, L. Giordano, Y. Yu, D. Fraggedakis, J. G. Sun, F. Maglia, R. Jung, M. Z. Bazant and Y. Shao-Horn, Revealing electrolyte oxidation via carbonate dehydrogenation on Ni-based oxides in Li-ion batteries by *in situ* Fourier transform infrared spectroscopy, *Energy Environ. Sci.*, 2020, **13**, 183–199.

35 Y. Li, W. Li, R. Shimizu, D. Cheng, H. Nguyen, J. Paulsen, S. Kumakura, M. Zhang and Y. S. Meng, Elucidating the Effect of Borate Additive in High-Voltage Electrolyte for Li-Rich Layered Oxide Materials, *Adv. Energy Mater.*, 2022, **12**(11), DOI: 10.1002/aenm.202103033.

36 W. Yao, M. Chouchane, W. Li, S. Bai, Z. Liu, L. Li, A. X. Chen, B. Sayahpour, R. Shimizu, G. Raghavendran, M. A. Schroeder, Y.-T. Chen, D. H. S. Tan, B. Sreenarayanan, C. K. Waters, A. Sichler, B. Gould, D. J. Kountz, D. J. Lipomi, M. Zhang and Y. S. Meng, A 5 V-class cobalt-free battery cathode with high loading enabled by dry coating, *Energy Environ. Sci.*, 2023, **16**, 1620–1630.

37 S. P. Ong, O. Andreussi, Y. Wu, N. Marzari and G. Ceder, Electrochemical Windows of Room-Temperature Ionic Liquids from Molecular Dynamics and Density Functional Theory Calculations, *Chem. Mater.*, 2011, **23**, 2979–2986.

38 T. Singh and A. Kumar, Static Dielectric Constant of Room Temperature Ionic Liquids: Internal Pressure and Cohesive Energy Density Approach, *J. Phys. Chem. B*, 2008, **112**, 12968–12972.

39 K. Paduszyński and U. Domańska, Viscosity of Ionic Liquids: An Extensive Database and a New Group Contribution Model Based on a Feed-Forward Artificial Neural Network, *J. Chem. Inf. Model.*, 2014, **54**, 1311–1324.

40 G. Petrella and A. Sacco, Viscosity and conductance studies in ethylene carbonate at 40 °C, *J. Chem. Soc., Faraday Trans. 1*, 1978, **74**, 2070.

41 M. Deguchi, D. Tazoe, Y. M. Todorov and K. Abe, Functional Electrolyte: Highly-Safe LIB Using Branched Carboxylic Acid Ester as Electrolyte Additive, *J. Electrochem. Soc.*, 2024, **171**, 040536.

42 M. S. Ding, Liquid Phase Boundaries, Dielectric Constant, and Viscosity of PC-DEC and PC-EC Binary Carbonates, *J. Electrochem. Soc.*, 2003, **150**, A455.

43 E. Frąckowiak and S. Kuksenko, The effect of 1,2-dimethoxyethane on the storage and performance of lithium cells with MnO_2 and (CF) cathodes, *J. Power Sources*, 1998, **72**, 174–177.

44 T. R. O'Toole, J. N. Younathan, B. P. Sullivan and T. J. Meyer, 1,2-Difluorobenzene: a relatively inert and noncoordinating solvent for electrochemical studies on transition-metal complexes, *Inorg. Chem.*, 1989, **28**, 3923–3926.

45 S. S. Zhang, K. Xu and T. R. Jow, Study of LiBF[sub 4] as an Electrolyte Salt for a Li-Ion Battery, *J. Electrochem. Soc.*, 2002, **149**, A586.

46 F. Larsson, P. Andersson, P. Blomqvist and B.-E. Mellander, Toxic fluoride gas emissions from lithium-ion battery fires, *Sci. Rep.*, 2017, **7**, 10018.

47 U. Heider, R. Oesten and M. Jungnitz, Challenge in manufacturing electrolyte solutions for lithium and lithium ion batteries quality control and minimizing contamination level, *J. Power Sources*, 1999, **81–82**, 119–122.

48 N. R. Park, M. Zhang, B. Han, W. Li, K. Qian, H. Nguyen, S. Kumakura and Y. S. Meng, Understanding Boron Chemistry as the Surface Modification and Electrolyte Additive for Co-Free Lithium-Rich Layered Oxide, *Adv. Energy Mater.*, 2024, **14**(46), DOI: 10.1002/aenm.202401968.

49 L. Qiao, U. Oteo, M. Martinez-Ibañez, A. Santiago, R. Cid, E. Sanchez-Diez, E. Lobato, L. Meabe, M. Armand and H. Zhang, Stable non-corrosive sulfonimide salt for 4-V-class lithium metal batteries, *Nat. Mater.*, 2022, **21**, 455–462.

50 H.-B. Han, S.-S. Zhou, D.-J. Zhang, S.-W. Feng, L.-F. Li, K. Liu, W.-F. Feng, J. Nie, H. Li and X.-J. Huang, Lithium bis(fluorosulfonyl)imide (LiFSI) as conducting salt for nonaqueous liquid electrolytes for lithium-ion batteries: Physicochemical and electrochemical properties, *J. Power Sources*, 2011, **196**, 3623–3632.

51 L. Wang, Z. Luo, H. Xu, N. Piao, Z. Chen, G. Tian and X. He, Anion effects on the solvation structure and properties of imide lithium salt-based electrolytes, *RSC Adv.*, 2019, **9**, 41837–41846.

52 L. J. Krause, W. Lamanna, J. Summerfield, M. Engle, G. Korba, R. Loch and R. Atanasoski, Corrosion of aluminum at high voltages in non-aqueous electrolytes

containing perfluoroalkylsulfonyl imides; new lithium salts for lithium-ion cells, *J. Power Sources*, 1997, **68**, 320–325.

53 H. Yoon, P. C. Howlett, A. S. Best, M. Forsyth and D. R. MacFarlane, Fast Charge/Discharge of Li Metal Batteries Using an Ionic Liquid Electrolyte, *J. Electrochem. Soc.*, 2013, **160**, A1629–A1637.

54 M. Ishikawa, T. Sugimoto, M. Kikuta, E. Ishiko and M. Kono, Pure ionic liquid electrolytes compatible with a graphitized carbon negative electrode in rechargeable lithium-ion batteries, *J. Power Sources*, 2006, **162**, 658–662.

55 M. Kerner, N. Plylahan, J. Scheers and P. Johansson, Ionic liquid based lithium battery electrolytes: fundamental benefits of utilising both TFSI and FSI anions?, *Phys. Chem. Chem. Phys.*, 2015, **17**, 19569–19581.

56 ROCO Global.

57 Y. Yang, D. M. Davies, Y. Yin, O. Borodin, J. Z. Lee, C. Fang, M. Olguin, Y. Zhang, E. S. Sablina, X. Wang, C. S. Rustomji and Y. S. Meng, High-Efficiency Lithium-Metal Anode Enabled by Liquefied Gas Electrolytes, *Joule*, 2019, **3**, 1986–2000.

58 S. Sheikh and A. H. Jahromi, Ionic liquids in green energy storage devices: lithium-ion batteries, supercapacitors, and solar cells, *Monatsh. Chem.*, 2024, **155**, 383–399.

59 X. Liu, A. Mariani, T. Diemant, X. Dong, P. Su and S. Passerini, Locally Concentrated Ionic Liquid Electrolytes Enabling Low-Temperature Lithium Metal Batteries, *Angew. Chem., Int. Ed.*, 2023, **135**(31), DOI: 10.1002/anie.202305840.

60 D. Hubble, D. E. Brown, Y. Zhao, C. Fang, J. Lau, B. D. McCloskey and G. Liu, Liquid electrolyte development for low-temperature lithium-ion batteries, *Energy Environ. Sci.*, 2022, **15**, 550–578.

61 M. Kerner, N. Plylahan, J. Scheers and P. Johansson, Ionic liquid based lithium battery electrolytes: fundamental benefits of utilising both TFSI and FSI anions?, *Phys. Chem. Chem. Phys.*, 2015, **17**, 19569–19581.

62 K. Yoshida, M. Nakamura, Y. Kazue, N. Tachikawa, S. Tsuzuki, S. Seki, K. Dokko and M. Watanabe, Oxidative-Stability Enhancement and Charge Transport Mechanism in Glyme–Lithium Salt Equimolar Complexes, *J. Am. Chem. Soc.*, 2011, **133**, 13121–13129.

63 P. G. Bruce and C. A. Vincent, Steady state current flow in solid binary electrolyte cells, *J. Electroanal. Chem. Interfacial Electrochem.*, 1987, **225**, 1–17.

64 S. Weng, X. Zhang, G. Yang, S. Zhang, B. Ma, Q. Liu, Y. Liu, C. Peng, H. Chen, H. Yu, X. Fan, T. Cheng, L. Chen, Y. Li, Z. Wang and X. Wang, Temperature-dependent interphase formation and Li+ transport in lithium metal batteries, *Nat. Commun.*, 2023, **14**, 4474.

65 K. Wen, L. Liu, S. Chen and S. Zhang, A bidirectional growth mechanism for a stable lithium anode by a platinum nanolayer sputtered on a polypropylene separator, *RSC Adv.*, 2018, **8**, 13034–13039.

66 C. M. Schott, P. M. Schneider, K.-T. Song, H. Yu, R. Götz, F. Haimerl, E. Gubanova, J. Zhou, T. O. Schmidt, Q. Zhang, V. Alexandrov and A. S. Bandarenka, How to Assess and Predict Electrical Double Layer Properties. Implications for Electrocatalysis, *Chem. Rev.*, 2024, **124**, 12391–12462.

67 C. S. Stefan, D. Lemordant, B. Claude-Montigny and D. Violleau, Are ionic liquids based on pyrrolidinium imide able to wet separators and electrodes used for Li-ion batteries?, *J. Power Sources*, 2009, **189**, 1174–1178.

68 R.-S. Kühnel, M. Lübke, M. Winter, S. Passerini and A. Balducci, Suppression of aluminum current collector corrosion in ionic liquid containing electrolytes, *J. Power Sources*, 2012, **214**, 178–184.

69 T. Ma, G.-L. Xu, Y. Li, L. Wang, X. He, J. Zheng, J. Liu, M. H. Engelhard, P. Zapol, L. A. Curtiss, J. Jorne, K. Amine and Z. Chen, Revisiting the Corrosion of the Aluminum Current Collector in Lithium-Ion Batteries, *J. Phys. Chem. Lett.*, 2017, **8**, 1072–1077.

70 W. Liu, J. Li, W. Li, H. Xu, C. Zhang and X. Qiu, Inhibition of transition metals dissolution in cobalt-free cathode with ultrathin robust interphase in concentrated electrolyte, *Nat. Commun.*, 2020, **11**, 3629.

71 K. Steinberg and B. M. Gallant, Revealing the Role of Lithium Carbonate at Lithium Metal Anodes Through Study of Gas-Reacted Interphases, *J. Electrochem. Soc.*, 2024, **171**, 080530.

72 E. W. C. Spotte-Smith, T. B. Petrocelli, H. D. Patel, S. M. Blau and K. A. Persson, Elementary Decomposition Mechanisms of Lithium Hexafluorophosphate in Battery Electrolytes and Interphases, *ACS Energy Lett.*, 2023, **8**, 347–355.

73 X. Liu, A. Mariani, M. Zarrabeitia, M. E. Di Pietro, X. Dong, G. A. Elia, A. Mele and S. Passerini, Effect of organic cations in locally concentrated ionic liquid electrolytes on the electrochemical performance of lithium metal batteries, *Energy Storage Mater.*, 2022, **44**, 370–378.

74 X. Liu, A. Mariani, T. Diemant, M. E. Di Pietro, X. Dong, P.-H. Su, A. Mele and S. Passerini, PFAS-Free Locally Concentrated Ionic Liquid Electrolytes for Lithium Metal Batteries, *ACS Energy Lett.*, 2024, **9**, 3049–3057.

75 J. Wan, M. Wan, X. Hou, F. B. Vangosa, D. Bresser, J. Li and E. Paillard, Combining ternary, ionic liquid-based, polymer electrolytes with a single-ion conducting polymer-based interlayer for lithium metal batteries, *Energy Mater.*, 2024, **4**(6), DOI: 10.20517/energymater.2024.50.

76 M. Palluzzi, A. Tsurumaki, H. Adenusi, M. A. Navarra and S. Passerini, Ionic liquids and their derivatives for lithium batteries: role, design strategy, and perspectives, *Energy Mater.*, 2023, **3**, 300049.

77 G. A. Heath, D. Ravikumar, B. Hansen and E. Kupets, A critical review of the circular economy for lithium-ion batteries and photovoltaic modules – status, challenges, and opportunities, *J. Air Waste Manage. Assoc.*, 2022, **72**, 478–539.

78 S. Nowak and M. Winter, The Role of Sub- and Supercritical CO_2 as "Processing Solvent" for the Recycling and Sample Preparation of Lithium Ion Battery Electrolytes, *Molecules*, 2017, **22**, 403.

79 P. A. Thomas and B. B. Marvey, Room Temperature Ionic Liquids as Green Solvent Alternatives in the Metathesis of Oleochemical Feedstocks, *Molecules*, 2016, **21**, 184.

80 J. F. Brennecke and B. E. Gurkan, Ionic Liquids for CO_2 Capture and Emission Reduction, *J. Phys. Chem. Lett.*, 2010, **1**, 3459–3464.

This journal is © The Royal Society of Chemistry 2025

Energy Environ. Sci., 2025, **18**, 8889–8906 | 8905

81 F. Karadas, M. Atilhan and S. Aparicio, Review on the Use of Ionic Liquids (ILs) as Alternative Fluids for CO_2 Capture and Natural Gas Sweetening, *Energy Fuels*, 2010, **24**, 5817–5828.

82 M. S. Shannon and J. E. Bara, Reactive and Reversible Ionic Liquids for CO_2 Capture and Acid Gas Removal, *Sep. Sci. Technol.*, 2012, **47**, 178–188.

83 Y. An, P. Zuo, X. Cheng, L. Liao and G. Yin, Preparation and Properties of Ionic-Liquid Mixed Solutions as a Safety Electrolyte for Lithium Ion Batteries, *Int. J. Electrochem. Sci.*, 2011, **6**, 2398–2410.

84 H. S. Dhattarwal and H. K. Kashyap, Heterogeneity and Nanostructure of Superconcentrated LiTFSI–EmimTFSI Hybrid Aqueous Electrolytes: Beyond the 21 m Limit of Water-in-Salt Electrolyte, *J. Phys. Chem. B*, 2022, **126**, 5291–5304.

85 M. Kunze, M. Montanino, G. B. Appetecchi, S. Jeong, M. Schönhoff, M. Winter and S. Passerini, Melting Behavior and Ionic Conductivity in Hydrophobic Ionic Liquids, *J. Phys. Chem. A*, 2010, **114**, 1776–1782.

86 R. Greil, J. Chai, G. Rudelstorfer, S. Mitsche and S. Lux, Water as a Sustainable Leaching Agent for the Selective Leaching of Lithium from Spent Lithium-Ion Batteries, *ACS Omega*, 2024, **9**(7), 7806–7816.

87 R. Goncalves, K. Titier, V. Latour, A. Peyré, N. Castaing, A. Daveluy and M. Molimard, Suitability of infrared spectroscopy for drug checking in harm reduction centres, *Int. J. Drug Policy*, 2021, **88**, 103037.

88 A. Stark, P. Behrend, O. Braun, A. Müller, J. Ranke, B. Ondruschka and B. Jastorff, Purity specification methods for ionic liquids, *Green Chem.*, 2008, **10**, 1152.

8906 | *Energy Environ. Sci.*, 2025, **18**, 8889–8906

This journal is © The Royal Society of Chemistry 2025